



UNIVERSITÀ POLITECNICA DELLE MARCHE
Repository ISTITUZIONALE

Experimental investigation by laser ultrasonics for high speed train axle diagnostics

This is the peer reviewed version of the following article:

Original

Experimental investigation by laser ultrasonics for high speed train axle diagnostics / Cavuto, A.; Martarelli, M.; Pandarese, G.; Revel, Gian Marco; Tomasini, Enrico Primo. - In: ULTRASONICS. - ISSN 0041-624X. - 55:1(2015), pp. 48-57. [10.1016/j.ultras.2014.08.010]

Availability:

This version is available at: 11566/223733 since: 2022-06-06T12:35:30Z

Publisher:

Published

DOI:10.1016/j.ultras.2014.08.010

Terms of use:

The terms and conditions for the reuse of this version of the manuscript are specified in the publishing policy. The use of copyrighted works requires the consent of the rights' holder (author or publisher). Works made available under a Creative Commons license or a Publisher's custom-made license can be used according to the terms and conditions contained therein. See editor's website for further information and terms and conditions.

This item was downloaded from IRIS Università Politecnica delle Marche (<https://iris.univpm.it>). When citing, please refer to the published version.

(Article begins on next page)

EXPERIMENTAL INVESTIGATION BY LASER ULTRASONICS FOR HIGH SPEED TRAIN AXLE DIAGNOSTICS

Alfonso Cavuto, Milena Martarelli, Giuseppe Pandarese, Gian Marco Revel, Enrico Primo
Tomasini

Original publication available at:

10.1016/j.ultras.2014.08.010

This manuscript version is made available under the CC-BY-NC-ND 4.0 license
<https://creativecommons.org/licenses/by-nc-nd/4.0/>



24 **Abstract**

25 The present paper demonstrates the applicability of a laser-ultrasonic procedure to improve the
26 performances of train axle ultrasonic inspection. The method exploits an air-coupled ultrasonic probe
27 that detects the ultrasonic waves generated by a high-~~power~~~~energy~~ pulsed laser. As a result, the
28 measurement chain is completely non-contact, from generation to detection, this making it possible
29 to considerably speed up inspection time and make the set-up more flexible. The main advantage of
30 the technique developed is that it ~~is working~~~~works~~ in thermo-elastic regime and it therefore can be
31 considered as a non-destructive method.

32 The laser-ultrasonic procedure investigated has been applied ~~for~~~~to~~ the inspection of a real high speed
33 train axle provided by the Italian railway company (Trenitalia), on which typical~~standard~~ fatigue
34 defects have been expressly created according to standard specifications.

35 A dedicated test bench has been developed so as to rotate the axle with the angle control -and to
36 speed up the inspection of the axle surface. The laser-ultrasonic procedure proposed can be
37 automated and is potentially suitable for regular inspection of train axles.

38 The main achievements of the activity described in this paper are:

- 39 - the study of the effective applicability of laser-ultrasonics for the diagnostic of train hollow
40 axles with variable sections by means of a numerical FE model,
- 41 - the carrying out of an automated experiment on a real train axle,
- 42 - the analysis of the sensitivity to experimental parameters, like laser source – receiving probe
43 distance and receiving probe angular position,
- 44 - the demonstration that the technique is suitable for the detection of surface defects purposely
45 created on the train axle.

46
47
48 **Keywords:** Laser-ultrasonics, NDT, air-coupled ultrasound, train axle, FE model

50 1. Introduction

51 Safety and reliability are two key issues in the railway field. Wheelset components, i.e. axle and
52 wheels, are often the main responsible for breakdowns and accidents, they being most subjected
53 either to static stress or fatigue. Although designed for unlimited life, they occasionally collapse
54 during operation because of the propagation of incipient cracks. Therefore their periodic inspection is
55 crucial. An open problem is, however, the estimation of the optimal inspection [frequency](#) intervals
56 (according to the concept of damage tolerance) [1] so as to increase safety without shortening the
57 periods between controls, this making it possible to reduce maintenance costs [2]. Currently periodic
58 inspection of axles is carried out by ultrasonic techniques using, for example, a number of rotating
59 contact probes, phased arrays or bore probes (for hollow axle diagnostics) [3, 4, 5].

60 Ultrasonic techniques, which are ~~a long established method~~ [well known in the state of the art](#), have
61 the disadvantage of requiring the probes to be in contact with the object to be investigated, which
62 lengthens the inspection time necessary to prepare the object and apply the coupling medium.
63 However, the typical problems of conventional techniques can be overcome by using a hybrid laser-
64 ultrasonic system based on the detection of ultrasonic waves generated by a high-~~power~~[energy](#)
65 pulsed laser via air-coupled ultrasonic transducers. Air-coupled ultrasound inspection has already
66 been successfully used in many industrial applications e.g. NDT on both thick [6] and thin [7]
67 composites, NDT on light thin historical vaults [8], density measurement of ceramic tiles [9], wood
68 detection [10], and thin metallic laminated [11, 12].

69 The hybrid system [here](#) proposed is completely non-invasive and it makes it possible to:

- 70 - overcome shape and accessibility problems,
- 71 - avoid the application of the coupling medium,
- 72 - shorten the inspection time for large surfaces.

73 Laser-ultrasonics has been applied in the aeronautical field for damage detection on thick composite
74 materials [13] and honeycombs [14] and in the railway field for rail [15,16], rail wheels [17] and axle
75 inspection [18]. Gonzales et al. [18] presented a Laser Air-Hybrid Ultrasonic Technique based on air
76 coupled ultrasounds. The ~~limitations~~ of the technique are due to the fact that it ~~is working~~works in
77 ablative regime and it exploits the Rayleigh waves reflected by the crack. Since that technique works
78 in ablative regime which damages the surface it cannot considered a non-destructive method. The use
79 of Rayleigh wave reflection makes it extremely difficult to ~~work~~deal with complex geometries,
80 ~~as~~like hollow axles with several section variations. In fact, the reflections due to the geometry can
81 overlap with the one induced by the crack and thus the desired signal can be buried into ~~the~~ noise. In
82 a very recent work the suitability of laser-ultrasonics for the inspection of wheelset flaws was proved
83 by means of a numerical study [19]. A numerical simulation with dynamic explicit integration was
84 presented, showing that the perturbation produced by the defect on the ultrasonic propagation, and
85 specifically on the surface or Rayleigh wave, is evident and therefore the technique is suitable for
86 diagnostic purposes.

87 The present paper shows the experimental application of laser ultrasonics ~~to~~for the inspection of a
88 real high speed train axle ~~provided~~supplied by the Italian railway company (Trenitalia), where
89 standard fatigue defects have been expressly created according to standard specifications.

90 The first aim of this work is to demonstrate that the technique works in ~~the~~ termo-elastic regime.
91 ~~Furthermore it~~It has been shownshows its functionality alsothat the technique can be applied also for
92 the inspection of complex geometries using direct Rayleigh waves. It ~~has been proved~~proves that
93 the technique can be applied also when the distance between laser source and ultrasound probe
94 exceeds 200 mm. Consequently it ~~is possible to apply it~~can be applied for the diagnostics of flaws
95 located in the fretting surface by ~~locating~~positioning the laser source and the ultrasound probe on
96 the opposite sides of the wheel press fitted area. That holding, the potentials of such technique for the
97 application to wheelsets are quite evident, as demonstrated by the results of the numerical model

98 presented in [19]. This would be the next step of the experimental investigation performed by the
99 authors.

100 The paper is structured in four Sections. Section 2 presents a numerical feasibility study performed
101 with the aim to verify the suitability of the technique proposed for axle flaw diagnostics. Such study
102 has been carried out by means of a numerical FE model simulating the generation of the thermo-
103 elastic displacement by a high-~~power~~~~energy~~ pulsed laser impinging on the material surface and the
104 propagation of the ultrasonic wave produced by the thermo-elastic effect within the material. The
105 numerical simulation has been used by the authors to design the experiments and optimize the
106 diagnostic procedure for flaw identification. The experimental set-up and the sensitivity analysis to
107 experimental parameters are reported in Section 3, and the results obtained in the tests are discussed
108 in Section 4.

109

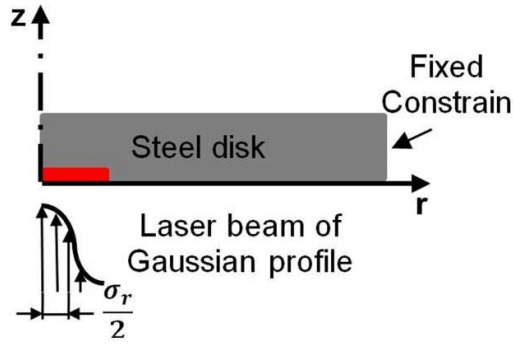
110 **2. Feasibility study of the Laser Ultrasonic technique by means of a numerical FE model**

111 In this section the finite element model developed for the design of the experiments based on laser
112 ultrasonics for the detection of flaws in a train axle is described. A coupled thermo-stress analysis
113 was exploited to simulate the generation and the propagation of Rayleigh waves and to drive the
114 experiments, by identifying the optimal testing parameters.

115 **2.1. Simulation of the elastic wave generation**

116 For the generation of the ultrasound wave from the pulsed laser excitation, a 2D axisymmetric model
117 simulating the half cross section of a steel disk with a radius of 20 mm and thickness of 3 mm was
118 developed.

119 Such undersized model makes it possible to optimize the numerical mesh and the input parameters
120 for an accurate simulation of the Rayleigh waves generation and to put the basis for the complete
121 model of the train axle.



122

123

Fig. 1. Schematic view of the numerical model.

124

Two different physics need to be considered in laser-ultrasonics: thermo-elasticity, for the ultrasonic wave generation due to the thermo-stress induced by the laser impulse [20, 21], and acoustics, for the ultrasonic wave propagation within the material [22]. Comsol Multiphysics software was used to carry out the numerical simulation. An implicit analysis with a generalized- α (alpha) time dependent-solver was implemented.

128

129

A convective cooling boundary condition ~~has been~~ was used on the top and bottom surface. Other boundaries were assumed to be thermally insulated. The body heat load within the steel disk is given by the following expression:

130

131

$$Q_{in}(r, z, t) = Q(t)(1 - R) \left(\frac{A_c}{\pi\sigma_r^2} \right) e^{-\left(\frac{r^2}{2\sigma_r^2}\right)} e^{-A_c z} \quad (1)$$

132

where σ_r is the standard deviation of the Gaussian laser beam. The value ~~assumed by~~ of σ_r in the model is 1.5 mm (for a laser beam ~~of~~ with a diameter of 6-mm). The steel thermal, mechanical and optical properties appearing in equation (1) and in the following equations (2) and (3) are reported in

133

134

135

Table 1. The variation ~~with temperature in~~ of the material properties ~~with temperature~~ was assumed to be low, when considering a thermo-elastic model with a heat flux lower than 16.9 MW/cm².

136

137

~~We assume~~ that The absorption of the laser pulse ~~on~~ at the surface of the steel sample ~~was assumed to~~ occurs without phase change and therefore the thermal properties of the metal are independent of

138

139 temperature [23]. The Young modulus ~~has been~~was considered to be varying linearly with ~~the~~
 140 temperature (about 0.15 GPa/K).

141

142 Table 1 Steel mechanical/thermal/optical properties.

ρ	Density	7900 kg/m ³
E	Young Modulus (@ 273.15 K)	200 GPa
C	Specific heat capacity	480 J/(kg K)
k	Thermal conductivity	50 W/(m K)
α	Coefficient of thermal expansion	10.7 e ⁻⁵ K ⁻¹
R	Reflection coefficient	0.3
A_c	Absorption coefficient	3.87 e ⁹ m ⁻¹

143

144 The time-dependence of the thermal power $Q(t)$ irradiated by the laser pulse is taken into account in
 145 equation (1) using a triangular function [24] with 12 ns of duration and an energy of 82 mJ. An
 146 integration time step of 4 ns was considered, thus leading to a sampling frequency of 250 MHz.

147 Equation (4) expresses the power density of the impinging laser beam absorbed by the material,
 148 depending on the reflectivity properties of its surface. The reflectivity was calculated analytically
 149 [23] according to the following equation:

$$R = \frac{2 - 2\xi + \xi^2}{2 + 2\xi + \xi^2} \quad (2)$$

150 where $\xi = \mu_0 \sigma c \delta$, and $c = 300\text{m/s}$ is the speed of light in vacuum, $\mu_0 = 4\pi 10^{-7} \text{ Hm}^{-1}$ is the magnetic
 151 permeability in vacuum, σ is the steel conductivity and δ is the skin depth. The skin depth can be
 152 estimated from the following equation:

$$\delta = (\pi \sigma \mu_r \mu_0 \nu)^{-1/2} \quad (3)$$

153 with μ_r the relative magnetic permeability and $\nu = 2.82 \times 10^{14} \text{ Hz}$ the radiation frequency at the IR
 154 wavelength of 1064 nm.

155 For the steel given in Table 1 $\mu_r = 1900$ and $\sigma = 7.04 \times 10^6 \text{ (}\Omega\text{m)}^{-1}$, thus $\delta = 0.258 \text{ nm}$, $\xi = 0.68$ and
156 $R = 0.3$.

157 The heat flux (Q) was estimated by knowing the laser energy (E), the pulse duration (τ) and the area
158 of the laser beam (A) corresponding to a laser beam of with a diameter of 6 mm, according to the
159 following equation:

$$Q = \frac{E}{\tau \cdot A} (1 - R) = \frac{0.082}{(12 \cdot 10^{-9}) \left(\frac{\pi}{4} \cdot 0.6^2\right)} 0.7 = 16.9 \frac{\text{MW}}{\text{cm}^2} \quad (4)$$

160
161 For a metallic material in the near infrared/visible wavelength region, the transition between the
162 thermo-elastic regime and ablative regime is governed by the laser power density absorbed by the
163 material [23]. For the steel given in Table 1 the transition value was calculated to be about 20
164 MW/cm^2 . Since the value of the thermal heat flux calculated with equation (4) is lower than 20
165 MW/cm^2 it can be stated that the ultrasound waves are generated in the thermal-elastic regime.

166 In order to investigate the effect of thermo-elastic expansion in terms of ultrasound wave
167 propagation, the solid-acoustic interaction was added. The acoustic model makes it possible to
168 connect the elastic wave propagation with the thermal deformation evaluated in the thermal stress
169 module. A prescribed displacement (in r and z directions, see Fig.1) boundary condition was set in
170 order to impose the thermal displacement, output of the thermal stress module, as the input of the
171 acoustic one.

172 A structured quadrilateral mesh with variable size was created. The element size varied between a
173 minimum value of 0.1 nm and a maximum of 1 μm . The minimum element size was set with the aim
174 to have some elements within the penetration area of the laser source. The penetration depth was
175 0.258 nm. The maximum element size was in agreement with the rule of $\lambda_r/10$ [25, 26], e.g. 0.29 mm
176 considering a frequency of 1 MHz and the shortest wavelength corresponding to Rayleigh wave
177 which travels at the speed of 2905 m/s.

178 An attenuation of ultrasonic waves of 4 neper/m was considered in the numerical model.

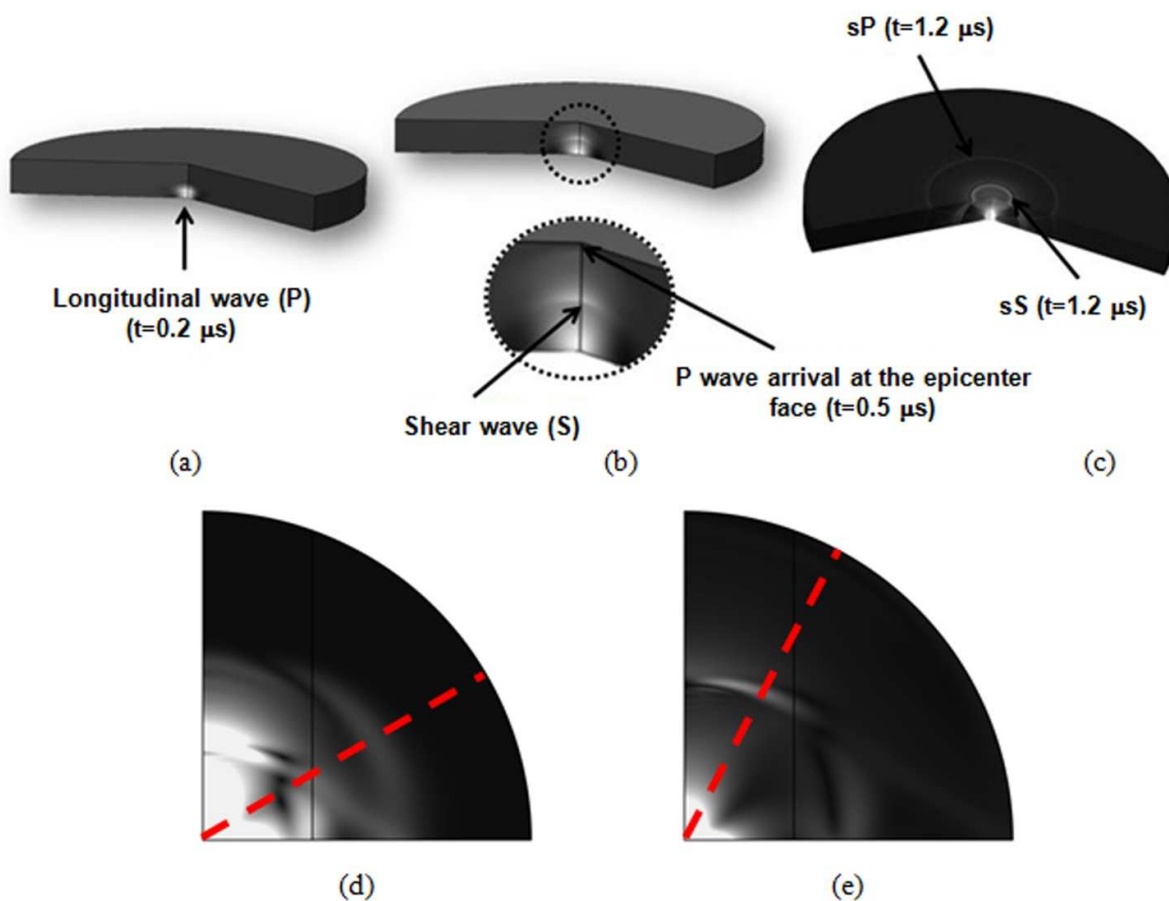
179 The simulation time was 5 μs , to detect all the phenomena implied in the process. The test sample

180 made for the model is shown Fig. 2, where the propagation of the different bulk waves is visible.

181 On the epicentriepicenter surface of the disk, see Fig. 2c, the surface skimming longitudinal (sP)

182 and shear (sS) waves are visible as well as at 1.2 μs . Those waves mark the intersection with the

183 epicentriepicenter surface of the disk with the longitudinal and shear wavefront [22].



184

185 *Fig. 2. 3D visualization of the propagation of the elastic waves: (a) Longitudinal (P) wave at $t=0.2$*

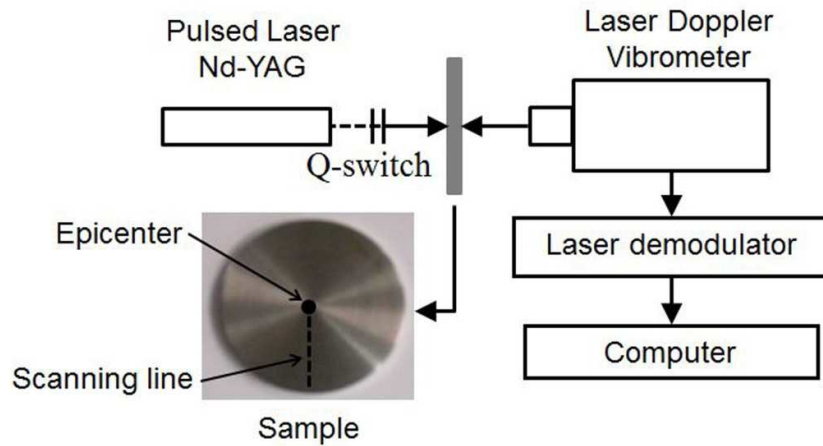
186 *μs . (b) P wave arrival at the epicentriepicenter face ($t=0.5$ μs) together with the arrival of the shear*

187 *wave (S) at the disk half thickness. (c) Surface skimming longitudinal (sP) and shear (sS) waves*

188 *($t=1.2$ μs). (d) ultrasound propagation at 0.3 μs , the P wave direction is evidenced by the dashed*

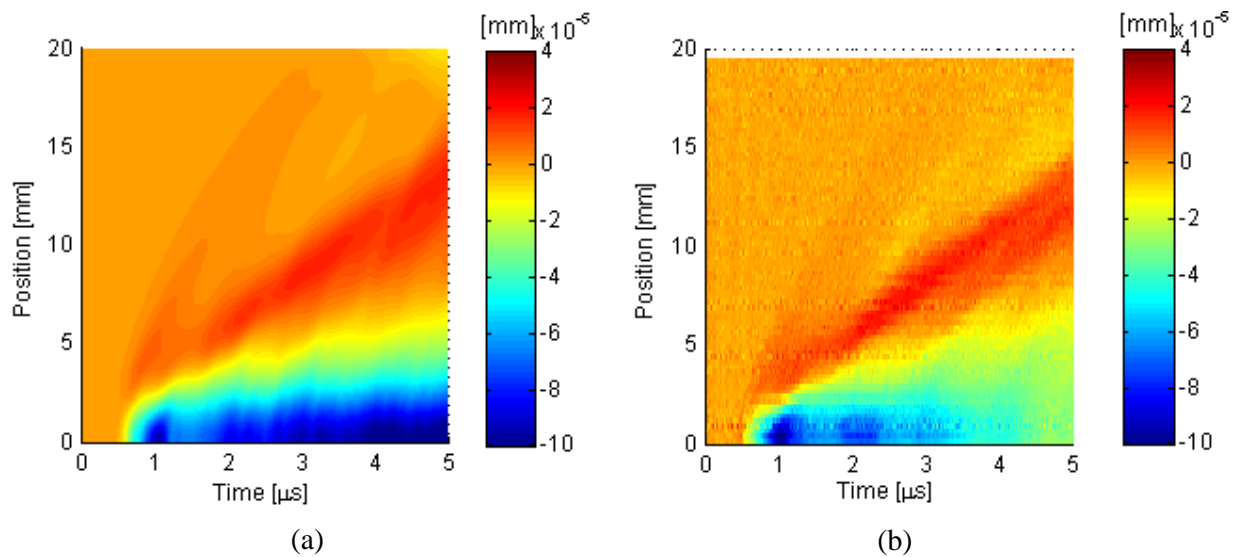
189 *line. (e) ultrasound propagation at 0.5 μs , the S wave is evidenced by the dashed line.*

190 The model was validated with experimental data, showing correspondence in terms of propagation
 191 mechanisms. The wave propagation was measured by a Laser Doppler Interferometer with a
 192 frequency bandwidth of 20 MHz (Fig. 3).



193 *Fig. 3. Experimental set-up.*

194 Fig. 4 shows the numerical and experimental B-scans respectively, i.e. the waterfall plot of the
 195 surface displacement in the z-direction with respect to time (in abscissa) and spatial position along
 196 the scanning line, reported in Fig. 3.



197 *Fig. 4. Waterfall of the numerical (a) and experimental (b) displacement in the z-direction.*

198

2.2. Simulation of the elastic wave propagation on a 2D axle section

The model developed for the Rayleigh wave generation from the pulsed laser source shown in the previous section was exploited on a more complex model, where a 2D axle section was simulated. The propagation of the elastic waves was modeled following the thermal diffusion and thermo-elastic displacement equations [22]:

$$\rho C \frac{\partial T}{\partial t} + \rho C \mathbf{u}_1 \nabla T = \nabla(k \nabla T) + Q \quad (5)$$

$$(\lambda + \mu) \nabla(\nabla \mathbf{u}_1) - \mu \nabla \times \nabla \times \mathbf{u}_1 - \rho \frac{\partial^2 \mathbf{u}_1}{\partial t^2} = \alpha(3\lambda + 2\mu) \nabla T \quad (6)$$

where T is the temperature rise in the metal, k is the thermal conduction coefficient, ρ is the density, C is the constant specific heat, $Q(r, z, t)$ is the power density of the heat source created by laser irradiation expressed in two-dimensional cylindrical coordinates (r, z) , α is the linear thermal expansion coefficient, λ and μ are the Lamé constants and \mathbf{u}_1 is the displacement vector due to the thermo-elastic effect.

The elastic wave equation is obtained from Newton's second law:

$$\rho \frac{\partial^2 \mathbf{u}_2}{\partial t^2} - \nabla \mathbf{s} = \mathbf{F}_v \quad (7)$$

where \mathbf{u}_2 is the displacement vector due to the elastic effect, \mathbf{s} is the stress tensor and \mathbf{F}_v represents the volume force vector. To study the propagation of Rayleigh waves with frequency components up to 1 MHz the shortest wavelength is given by:

$$\lambda_r = \frac{c_r}{f} = \frac{2905 \cdot 10^3}{1 \cdot 10^6} = 2.90 \text{ mm} \quad (8)$$

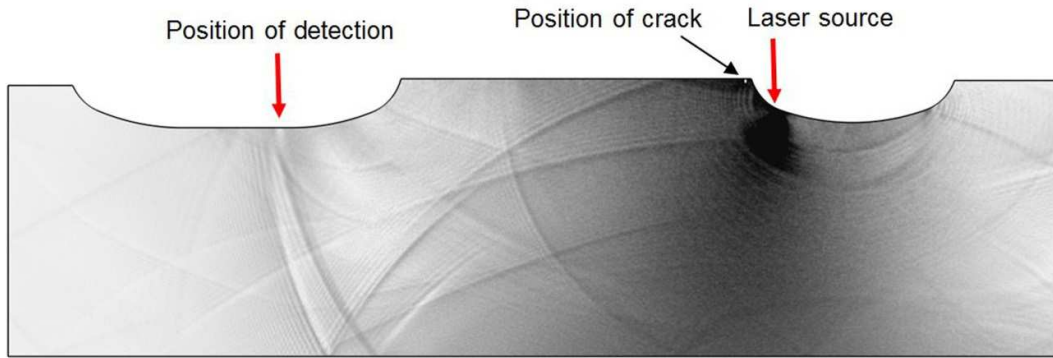
The Rayleigh velocity was measured experimentally, it resulting in 2905 m/s.

A quadrilateral mesh was used. The size of the finite elements was chosen in order to have a [sufficiently suitable](#) spatial resolution of the propagating waves. In [25, 26] it is recommended to have at least 10 nodes per wavelength and therefore the element size must be at least 1/10 of the shortest

218 | wavelength to be analyzed, i.e. smaller than $l_e = \lambda_r / 10 = 0.29 \text{ mm}$, where λ_r is the Rayleigh
219 | wavelength.

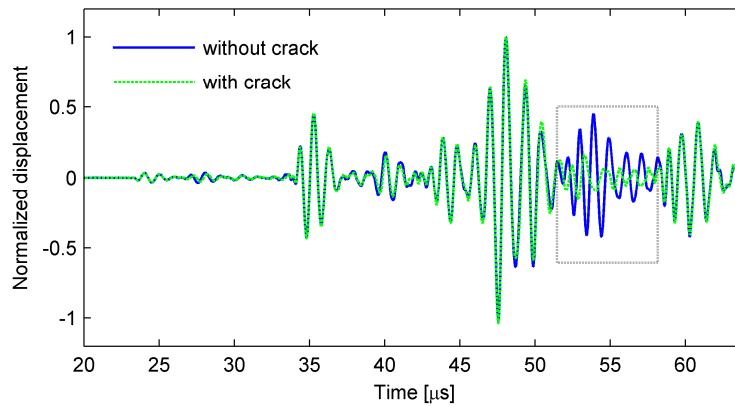
220 | The model made it possible to simulate the propagation of the elastic wave within the axle section
221 | and to verify that the Rayleigh wave would not ~~attenuate and~~ bury into the floor noise when traveling
222 | long distances, like the press fitting areas where the wheel sits. Besides, the model aimed at proving
223 | that the presence of a flaw in the path traveled would produce a perturbation on the Rayleigh wave
224 | which could be detected by an ultrasound transducer. In Fig. 5 the propagation of the elastic waves
225 | within the 2D axle section and their interference with a flaw are presented. Fig. 6 shows the
226 | ultrasound signals that could be acquired by a transducer placed on the opposite side of the press
227 | fitting area (red arrow on the left in Fig. 5) with respect to the pulsed laser impinging point (red
228 | arrow on the right in Fig. 5). In the model the distance between the laser impinging position and the
229 | detection one has been set to 143.5 mm that corresponds to 154 mm distance along the axle profile.
230 | The two signals reported in Fig. 6 were obtained by running the model with and without a crack of
231 | 1.1 mm length and 1 mm depth located at 11.5 mm with respect to the laser impinging position, as
232 | shown in Fig. 5. The waveforms calculated on the undamaged and damaged configurations have
233 | been filtered on the frequency range of the ultrasound probe used in the experiments ($1 \text{ MHz} \pm 200$
234 | kHz) and they have been plotted with normalized amplitude. The attenuation produced by the flaw is
235 | evident and it is of 7.3 dB, which was determined as the ratio of the undamaged signal RMS value
236 | and the damaged signal RMS value. The RMS was calculated in a time window centered on the
237 | Rayleigh wave time of arrival. That window is represented by the gray box illustrated in Fig. 6. An
238 | attenuation of 7.3 dB can be detected by an ultrasound transducer, as it will be demonstrated
239 | experimentally in Section 3, where the attenuation produced by the defect is of the same order of
240 | magnitude as the one calculated with the model.

241



242
243

Fig. 5. Propagation of the elastic waves in the 2D axle section and their interference with the flaw.



244

245

Fig. 6. Displacement waves with crack and without crack at the position of detection.

246

3. Experimental set-up

247

3.1. Test item

248

The test item is a train axle, Fig. 7a, on which typical fatigue defects were created. In practice four

249

convex defects were machined on the external surface, see Fig. 7b, two of them in the wheel fitting

250

area (D1 and D3) and the other two in the section transition (D2 and D4). The defect morphology is

251

reported in Table 2.

252

Table 2 Defect morphology.

Defects	Size of defect		
	H (mm)	L (mm)	D Max depth (mm)
D1	31	1.1	1
D2	28	1.1	1
D3	28	1.1	1
D4	28	1.1	1

253

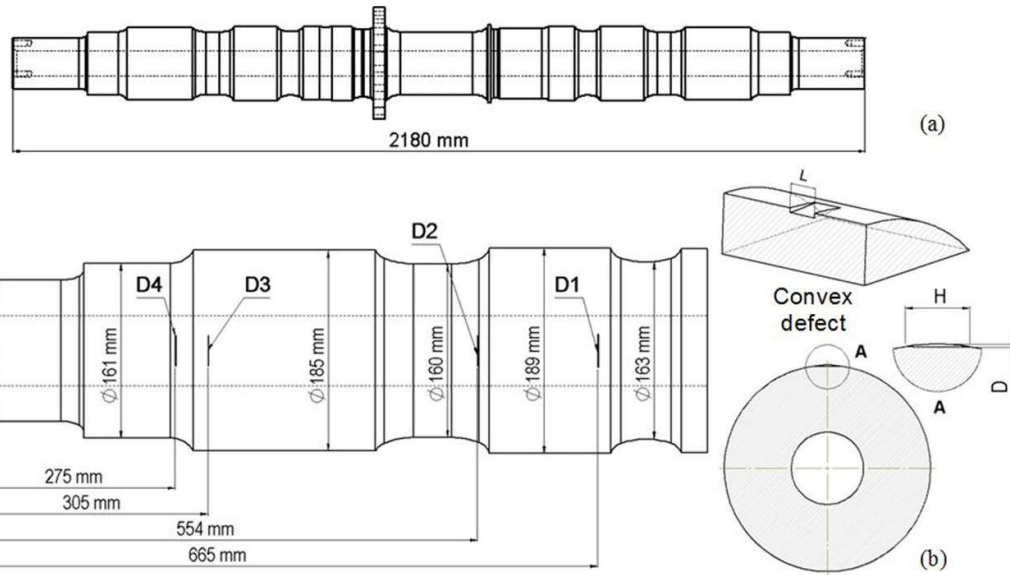
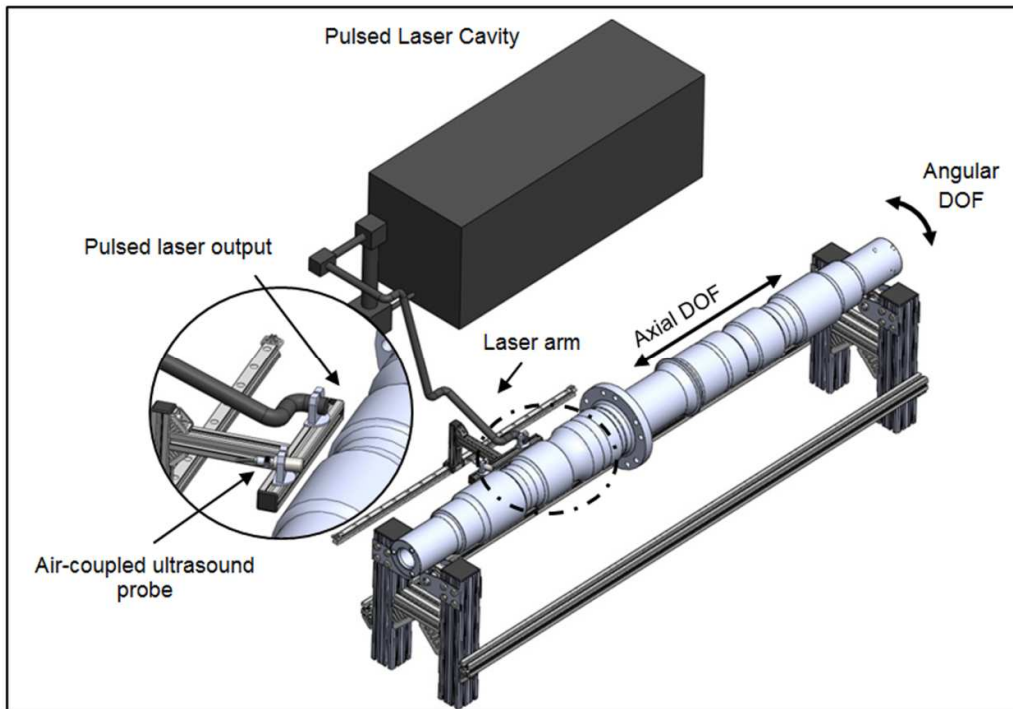


Fig. 7. Test item (a) and defect positions (b).

3.2. Test bench

The train axle was mounted on a support that made it possible to control its rotation, in order to be able to scan the axle surface along a circumference. The probes were installed on a frame where they could move along the axial direction. Therefore the complete lateral surface of the axle could be inspected by the laser ultrasonic system, see Fig. 8.

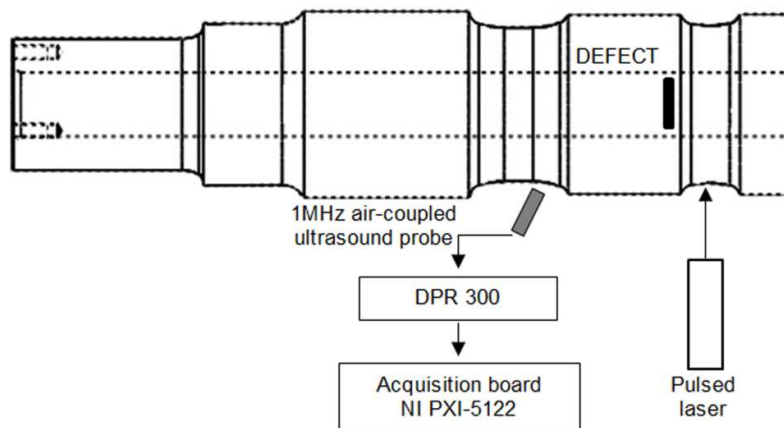
The laser ultrasonic system was made up of a pulsed laser source, a Nd-Yag IR laser (1064 nm), pulses of 12 ns duration and 82 mJ energy, from Continuum, and a 1 MHz air-coupled ultrasound piezoelectric probe from Ultran Group (model NCT210, with 8 mm diameter of active area). The ultrasound probe conditioning system was a DPR 300 Pulser/Receiver from JSR Ultrasonics. The ultrasound signals were amplified with a gain level of 69 dB and acquired with a high speed Digitizer board NI PXI-5122 (100 MHz bandwidth). The laser beam was guided towards the axle under test by means of an arm connected to the pulsed laser cavity as shown in Fig. 8.



268

269

Fig. 8. Scheme of the laser-ultrasonic scanning system.



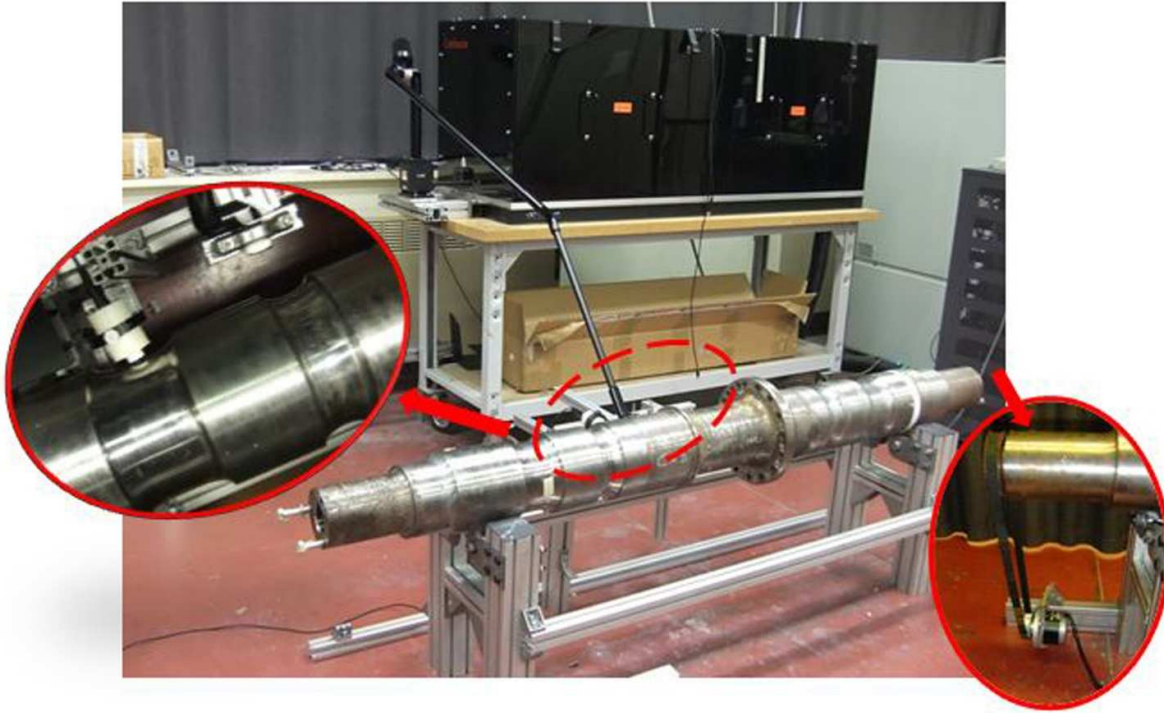
270

271

Fig. 9. The laser-ultrasonic experimental set-up.

272 The laser ultrasonics system was installed with the laser source and receiving probe far apart, in
 273 order to point outside-out of the wheel fitting surface, as shown in Fig. 9. A collimated laser beam
 274 with a diameter of about 8.5 mm was used to keep the ultrasonic waves generation within a thermo-
 275 elastic regime.

276 | The axle was made to rotate by an electric motor and the rotation angle was measured by an
277 | integrated encoder. A circumferential scan was performed along an angle of 93 deg with an angular
278 | resolution of 1.5 deg. The real setup is shown in Fig. 10.



279

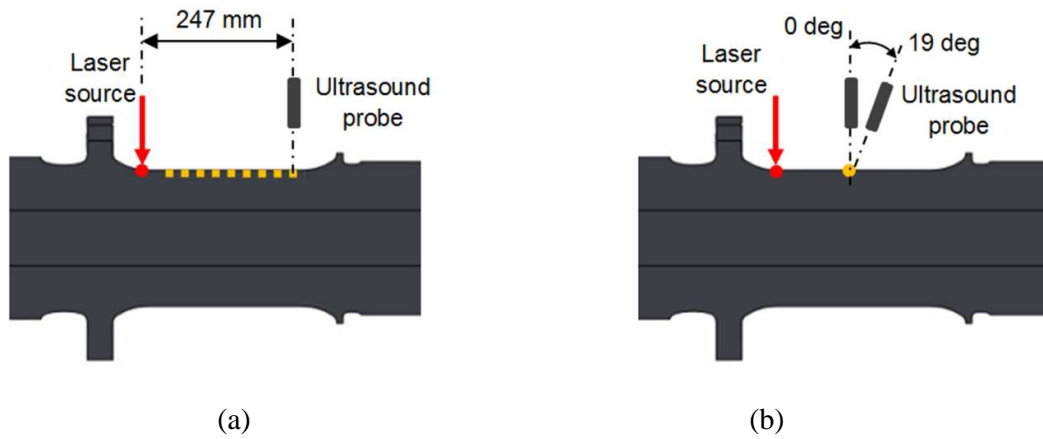
280

Fig. 10. The laser-ultrasonic scanning system.

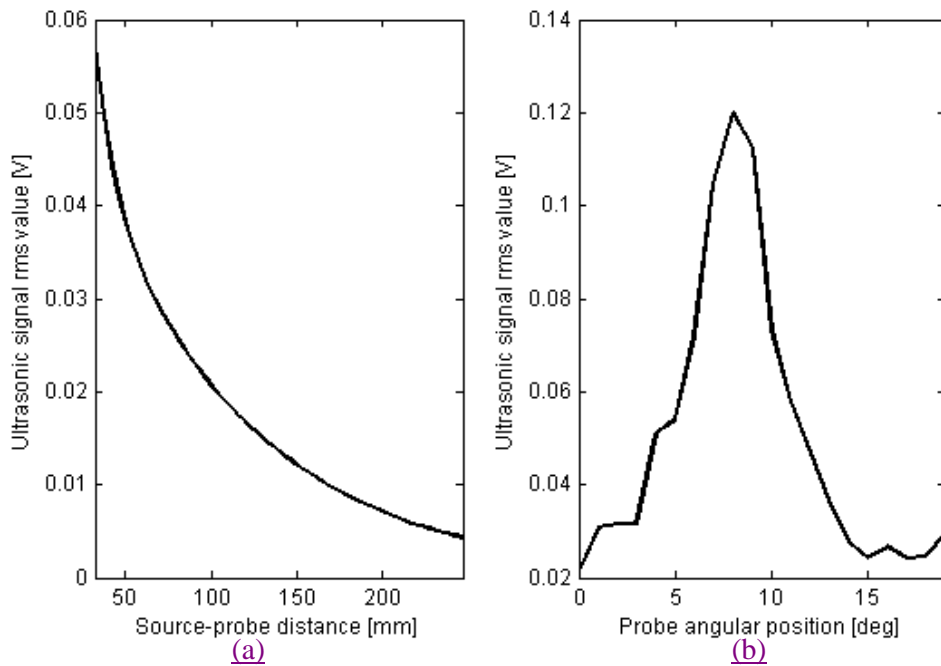
281 **3.3. Analysis of the sensitivity to experimental parameters**

282 The aim of the experimental technique proposed in this paper is to be able to acquire a consistent
283 signal even at a long distance from the laser source and therefore to make it possible to perform the
284 measurement by pointing the laser source and the ultrasound probe above and beyond the press fitted
285 zones of the axle, respectively. In order to verify the operation of the laser-ultrasonic technique in
286 dependence of the source-probe distance, a sensitivity analysis to this particular parameter was
287 performed. In practice, the ultrasound probe was moved along the axle surface starting from a
288 distance of 32 mm up to 247 mm, with a spatial resolution of 5 mm, (see Fig. 11a) and the RMS of
289 the signal acquired plotted again the sound-probe distance (see Fig. 12a). The probe angle used in

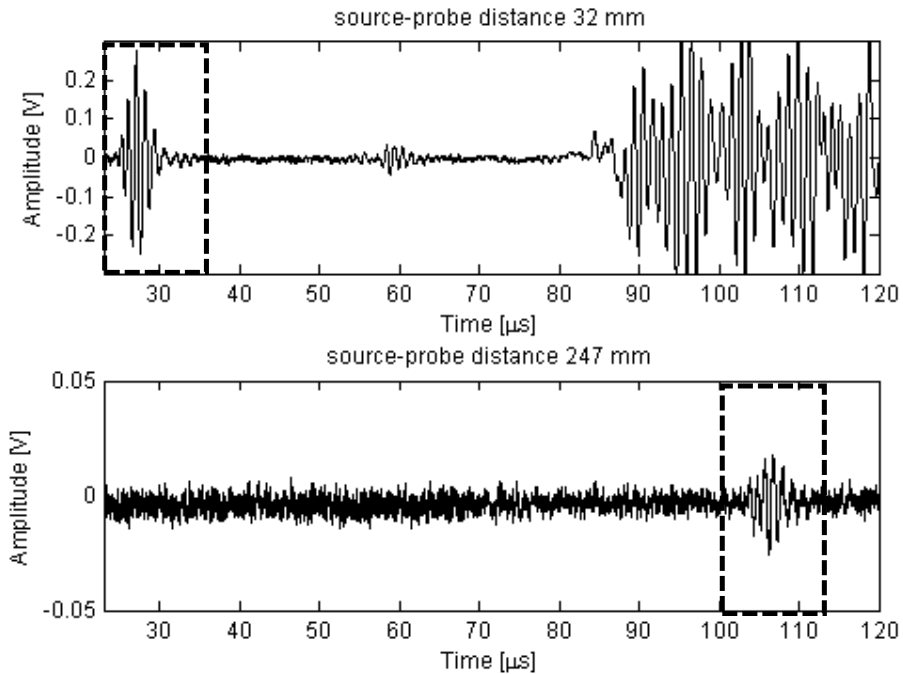
290 this analysis was of 6 deg. It is clear that the RMS decreases with the distance but, when comparing
 291 the ultrasound time history acquired at 32 mm with the one acquired at 247 mm (see Fig. 13, where
 292 the Rayleigh waves are highlighted by the dashed box), the arrival of the Rayleigh wave is still
 293 evident: its SNR is 12.5 dB.



296 | *Fig. 11. The laser ultrasonic experimental set-up for the sensitivity analysis to source-probe distance*
 297 | *(a) and probe angular position (b).*



299 Fig. 12. Ultrasonic signal RMS variation with respect to source-probe distance (a, probe angular
300 position 6 deg) and probe angular position (b, source-probe distance 32 mm).



301
302 Fig. 13. Ultrasonic time history at the minimum (32 mm, dashed line) and the maximum (247 mm,
303 solid line) source-probe distance.

304 A sensitivity analysis to the angular position of the ultrasound probe axis with respect to the normal
305 of the axle surface was then performed. The probe was placed at 32 mm from the laser source and,
306 starting from an angle of 0 deg, where the probe axis was normal to the axle surface, it was tilted up
307 to 19 deg with a resolution of 0.5 deg. As it is evident in Fig. 12b, the optimal angular position was
308 at about 8 deg, according to Snell's law [27].

309 4. Analysis of results

310 For each configuration, a series of ultrasound time histories with a duration of 500 μs was acquired at
311 every scanning position along the arc considered. The attention was focused on the Rayleigh wave
312 propagation, it being the most sensitive elastic wave to the presence of the defect. Moreover, because

313 of the geometry complexity and of the generation of elastic waves by the laser-material interaction,
314 the Rayleigh wave is also the most efficient for surface defect identification.

315 The experimental set-up (i.e. laser and probe positions), the axle section tested and the defect
316 location (D1) are shown in Fig. 14c. The time history acquired in the first scanning position is plotted
317 in Fig. 14a. A close up around the time of arrival of the bulk waves is given in Fig. 14b: that time
318 history evidences the Rayleigh wave arrival time at about 75 μ s. However, other waves are visible in
319 the waveform which are reflections of longitudinal and shear waves due to the geometry complexity
320 (section transitions).

321 The B-scan close-up around the Rayleigh wave time of arrival, shown in Fig. 15, evidences the
322 presence of the defect, which produces a strong attenuation ~~and delay~~ of the Rayleigh wave itself.

323 The same plots given for defect D1 are reported for the other defects (D2, D3 and D4 respectively) in
324 Fig. 16. Again, the Rayleigh wave ~~highlighted in the time histories and in the B-scans~~, evidences
325 the presence of the defect. It should be noticed that the experimental set-ups of both defects D1 and
326 D2 are similar: the distance between the pulsed laser and the air-coupled ultrasound probe is the
327 same and therefore the Rayleigh time of arrival is equal, ~~of~~ about 75 μ s. The same occurs for defects
328 D3 and D4, where the distance between the pulsed laser and the air-coupled ultrasound probe is
329 larger and therefore the Rayleigh time of arrival is of about 87 μ s.

330

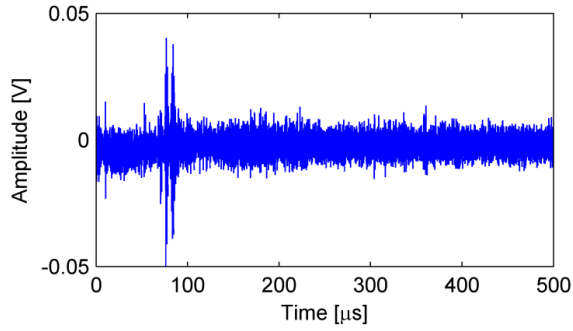
331

332

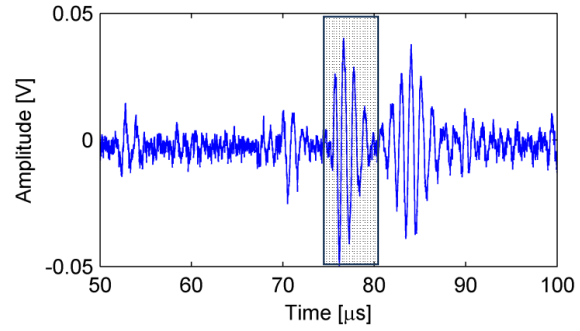
333

334

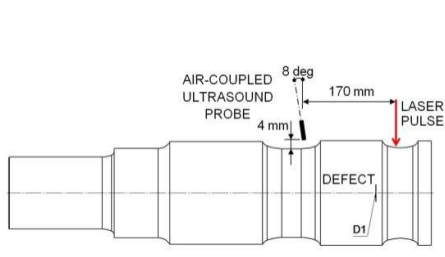
335



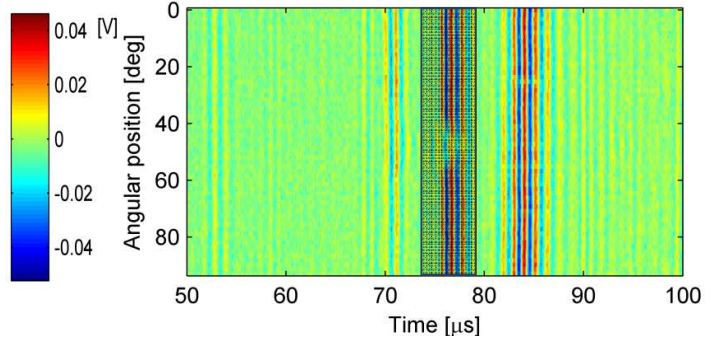
(a) Entire time history



(b) Time history close-up on the bulk waves



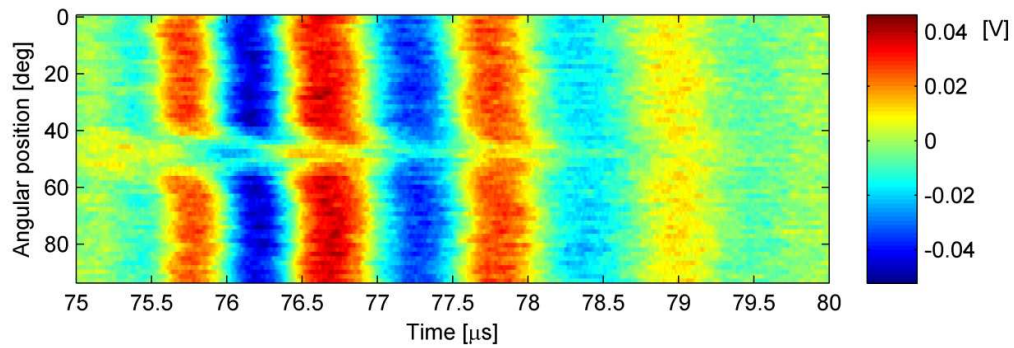
(c) Experimental set-up



(d) B-scan

336

Fig. 14. Time histories (a) and (b), experimental set-up scheme (c) and B-scan (d) – D1.



337

338

Fig. 15. B-scan close-up around the Rayleigh wave time of arrival – Defect D1.

339

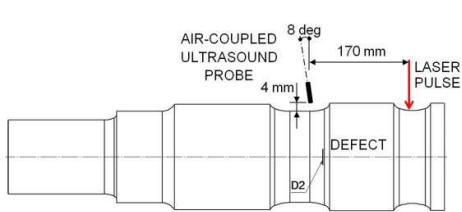
340

341

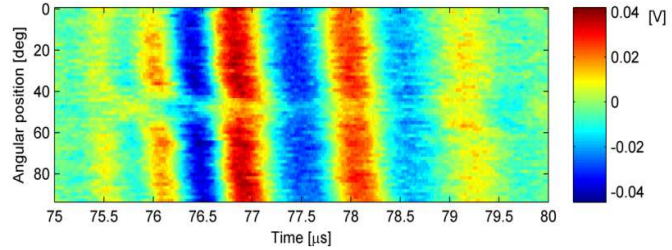
342

343

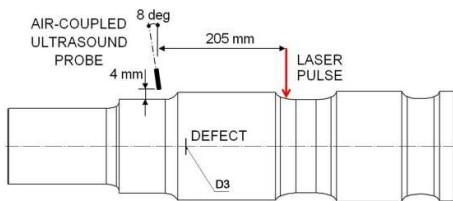
344



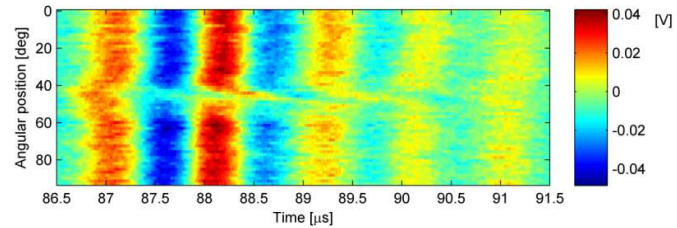
(a) Experimental set-up - defect D2



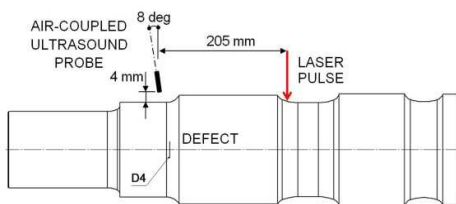
(b) B-scan of defect D2



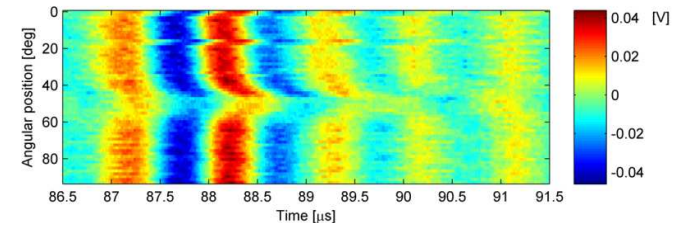
(c) Experimental set-up - defect D3



(d) B-scan of defect D3



(e) Experimental set-up - defect D4



(f) B-scan of defect D4

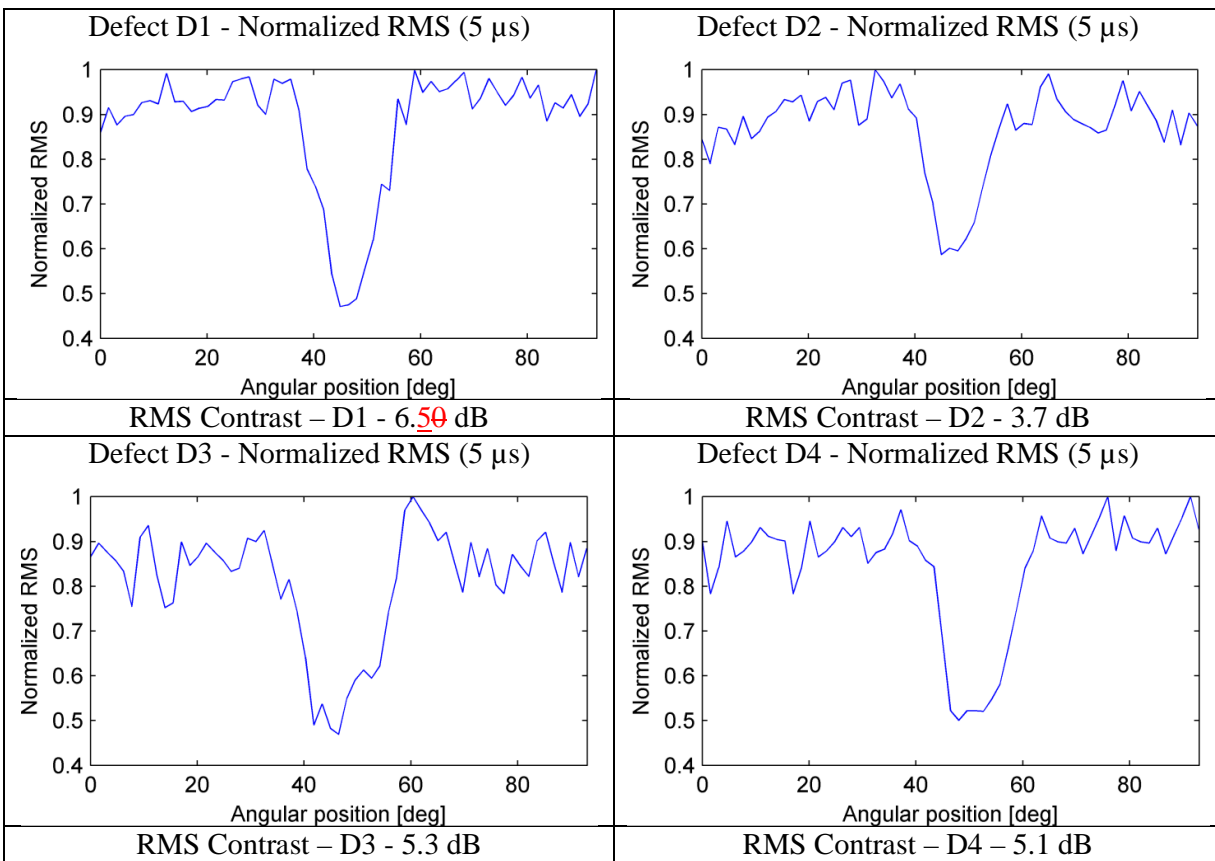
345 *Fig. 16. Experimental set-up scheme (a), (c), (e) and B-scan (b) (d), (f) for defects D2, D3, D4*
 346 *respectively.*

347 The RMS plots over the time axis (abscissa) of the B-scans obtained for the four defects were
 348 calculated and compared in Table 3. Those plots were normalized against the maximum RMS value
 349 of each plot. The contrast between the RMS in the damaged and in the undamaged areas is presented
 350 also in Table 3, which was calculated considering the minimum values of the RMS (in the damaged
 351 area) and the floor values RMS (in the undamaged area). It is clear that the best contrast between the
 352 undamaged area and the damaged one occurs for defect D1 (6.5 dB), where the pulsed laser is close
 353 to the defect. On the other hand, it is possible to see that the contrast between the undamaged area
 354 and the damaged one undergoes a drop when the defect is far from the laser source, which is the case
 355 of defects D2, D3 and D4. The worst contrast occurred for defect D2 and it is due to the fact that the
 356 receiving probe is located after a very sharp transition, this strongly attenuating the ultrasound wave
 357 propagation (e.g. it is evident that the signal minimum is lower than the other ones). Concerning

358 defects D3 and D4, instead, the receiving probe is located after a smoother transition, this reducing
 359 the attenuation of the ultrasound waves.

360 The attenuation measured experimentally confirms the result achieved with the model exploited in
 361 Section 2 for the feasibility study, where a 7.3 dB attenuation was calculated. The order of magnitude
 362 of the attenuation is comparable, although despite the differences exist between the numerical and
 363 experimental data, e.g. the experimental signals are acquired with air-coupled transducers while the
 364 numerical model does not take propagation in air into account ~~propagation in air~~.

365 Table 3 Normalized RMS and Damaged/Undamaged RMS Contrast.



366

367 5. Conclusions

368 The paper has shown the applicability of laser-ultrasonics, a non-destructive, non-contact technique,
 369 for the inspection of train axles. The main advantage of the proposed technique with respect to the
 370 state of the art is that it operates in thermo-elastic regime and therefore it can be considered a non-

371 destructive method. ~~A further advantage is that the crack produces an attenuation~~ Furthermore, it is
372 ~~based on the fact that the crack produces an attenuation~~ of the direct Rayleigh wave. That wave can
373 be generally distinguished from the reflections produced by the geometry and therefore it can be used
374 as defect classification feature also with very complex geometries.

375 Four convex defects typically generated by fatigue on the external surfaces of an axle have been
376 investigated. Two of the defects were on a transition section and the other two on a wheel fitting
377 area. All the defects have been identified by observing the Rayleigh wave propagation, it presenting
378 an evident attenuation when passing through the damaged area. The contrast between the undamaged
379 area and the damaged one made it possible to identify the complete set of defects, although it has
380 been evidenced that the best situation occurs when the defect is close to the laser, i.e. the ultrasound
381 waves source, where the contrast reaches 6.5 dB.

382 The good results achieved with the experimental procedure proposed in this paper incentivized the
383 authors to extend the application to axles mounted on a complete wheelset, with the aim to prove its
384 suitability for the remote inspection of railway axles in service.

385 **ACKNOWLEDGEMENTS**

386 The authors wish to thank Trenitalia S.p.A. Direzione Tecnica - Ingegneria Rotabili e Tecnologie di
387 Base and specifically Luca Labbadia and Marco Sarti for their precious contribution and for
388 providing the train axle. The authors wish to thank also Antonio D'Antuono for his valuable
389 contribution to the development of the numerical FE model. The work has been financed by the
390 National Ministry of Education, University and Research within a National Project PRIN
391 2009PSJW8Z "Development of a laser-ultrasonic system for non-destructive-testing aiming at
392 improving railway safety".

393

394

395 **REFERENCES**

- 396 [1] M. Carboni, S. Cantini, A new approach to the definition of “Probability of Detection” curves,
397 Proceeding of 10th European Conference on Non-Destructive Testing (ECNDT10), (2010),
398 Moscow, Russia.
- 399 [2] M. Carboni, J. Rudlin, Analysis and determination of UT POD curves for railway axles,
400 Proceeding of 3rd International Conference Reliability, Safety and Diagnostics of transport
401 structures and means, (2008) Pardubice, Czech Republic, 11-18.
- 402 [3] Railway applications - In-service wheelset operation requirements - In-service and off-vehicle
403 wheelset maintenance, in EN 15313.
- 404 [4] Non-destructive testing - Ultrasonic examination – Parts 1-6, in UNI EN 583-1: 2004.
- 405 [5] S. Cantini, G. Patelli, S. Beretta, M. Carboni, Assessment of Safe Life Inspection Intervals for
406 Forged Axles/Rotors: The Influence of In Service NDT Reliability (POD curve), Proceeding of
407 7th European Congress of Joining Technology (Eurojoin7), (2009), Venice, Italy, CD-ROM (13
408 pages).
- 409 [6] G.M. Revel, G. Pandarese, A. Cavuto, Advanced ultrasonic non destructive testing for damage
410 detection on thick and curved composite elements for constructions, Journal of Sandwich
411 structures and Material, 15(1) (2013): 1-20, DOI 10.1177/1099636212456861.
- 412 [7] P. Pietroni, G.M. Revel, Non contact ultrasonic techniques for composite material diagnostics in
413 aeronautics applications, Proceeding of 9th European Conference on Non-Destructive Testing,
414 Berlin, 25-29 September 2006.
- 415 [8] E. Quagliarini, G.M. Revel, S. Lenci, E. Seri, A. Cavuto, G. Pandarese, Historical plasters on
416 light thin vaults: State of conservation assessment by a Hybrid ultrasonic method. Journal of
417 Cultural Heritage, 15 (2014) 104–111.
- 418 [9] G.M. Revel, Measurement of the apparent density of green ceramic tiles by a non-contact
419 ultrasonic method, Experimental Mechanics, 47(5) (2007) 637-48.

- 420 [10]M. R. Fleming, M. C. Bhardwaj, J. J. Janowiak, J.E. Shield, R. Roy, D.K. Agrawal, L. S. Bauer,
421 D.L. Miller, K. Hoover, Noncontact ultrasound detection of exotic insects in wood packing
422 materials, *Forest Products Journal*, June 2005.
- 423 [11]D.W. Schindel, Air-coupled generation and detection of ultrasonic bulk waves in metals using
424 micromachined capacitance transducers, *Ultrasonics* 35 (1997) 1799-181.
- 425 [12]W.M.D. Wright, D.A. Hutchins, Air-coupled ultrasonic testing of metals using broadband pulses
426 in through-transmission, *Ultrasonics* 37 (1999) 19–22.
- 427 [13]D. Cerniglia, B.B. Djordjevic, V. Nigrelli, Quantitative subsurface defect detection in composite
428 materials using a non-contact ultrasonic system, *IEEE Ultrasonics Symposium*, (2001) 751-754.
- 429 [14]C. Cosenza, D. Cerniglia, B.B. Djordjevic, Non-contact ultrasonic inspection of skin/core bond in
430 honeycomb with Lamb waves, *IEEE Ultrasonics Symposium*, Monaco (2002).
- 431 [15]S. Kenderian, B.B. Djordjevic, Jr. R.E. Green, Laser-based and air-coupled ultrasound as
432 noncontact and remote techniques for testing railroad tracks, *Materials Evaluation* 60 (1) (2002)
433 65-70.
- 434 [16]D. Cerniglia, S. Kenderian, B.B. Djordjevic, G. Garcia, R. Morgan, Laser e trasduttore di
435 accoppiamento in aria per l'ispezione ultrasonica non a contatto nel settore ferroviario,
436 Conferenza AIPnD, Matera, Italy (2002).
- 437 [17]S. Kenderian, D. Cerniglia, B. B. Djordjevic, G. Garcia, Laser-air hybrid ultrasonic technique
438 for dynamic railroad inspection application, *Proceedings of 16th WCNDT 2004 - World*
439 *Conference on NDT*.
- 440
441 [18]K. Gonzales, S. Kendarian, D. Carter, A Smith, R Morgan, Non-contact interrogation of railroad
442 axles using laser-based ultrasonic inspection, *proceedings of JRC2005*, Pueblo, Colorado. DOI:
443 10.1109/RRCON.2005.186070.
- 444 [19]C. Mineo, D. Cerniglia, A. Pantano, Numerical study for a new methodology of flaws detection
445 in train axles, *Ultrasonics* (2013), <http://dx.doi.org/10.1016/j.ultras.2013.10.008>.

- 446 [20]P. Castellini, G.M. Revel, L. Scalise, R.M. De Andrade, Experimental and numerical
447 investigation on structural effects of laser pulses for modal parameter measurement, *Optics and*
448 *Lasers in Engineering* 32(6) (2000) 565-581.
- 449 [21]P. Castellini, G.M. Revel, L. Scalise, Measurement of vibrational modal parameters using laser
450 pulse excitation techniques, *Measurement* 35 (2004) 163-179.
- 451 [22]J. Wanga, Z. Shen, B. Xu, X. Ni, J. Guan, J. Lu, Numerical simulation of laser-generated
452 ultrasound in non-metallic material by the finite element method, *Optics & Laser Technology* 39
453 (2007) 806–813.
- 454 [23]C.B. Scruby, L.E. Drain, *Laser Ultrasonics: Techniques and Applications*, CRC Press, 1990.
- 455 [24] E. Lacatus, M.A. Sopronyi, G.C. Alecu, A. Tudor, Heat Transfer and Phase Transformation
456 on Matrix Assisted Pulsed Laser Evaporation (MAPLE) of Biocompatible Thin Layers,
457 *Proceedings of 2013 Comsol Conference*, Rotterdam.
- 458 [25]D. Cerniglia, A. Pantano, C. Mineo, Influence of laser beam profile on the generation of
459 ultrasonic waves, *Appl. Phys. A*. 105 (2011) 959–967.
- 460 [26]D. Alleyne, P. Cawley, A two-dimensional Fourier transform method for measurement of
461 propagating multimode signals. *Journal of the Acoustical Society of America* 89 (3) (1991)
462 1159–68.
- 463 [27] I. Solodov, D. Döring, G. Busse, Air-Coupled Lamb and Rayleigh Waves for Remote NDE of
464 Defects and Material Elastic Properties, *Journal of Mechanical Engineering* 56 (9) (2010) 557-
465 564.

466

467 **Figure captions**

468 Fig. 1. Schematic view of the numerical model.

469 Fig. 17. 3D visualization of the propagation of the elastic waves: (a) Longitudinal (P) wave at $t=0.2$
470 μs . (b) P wave arrival at the epicenter face ($t=0.5 \mu\text{s}$) together with the arrival of the shear wave (S)

471 at the disk half thickness. (c) Surface skimming longitudinal (sP) and shear (sS) waves ($t=1.2 \mu\text{s}$).

472 (d) ultrasound propagation at $0.3 \mu\text{s}$, the P wave direction is evidenced by the dashed line. (e)

473 ultrasound propagation at $0.5 \mu\text{s}$, the S wave is evidenced by the dashed line.

474 Fig. 3. Experimental set-up.

475 Fig. 4. Waterfall of the numerical (a) and experimental (b) displacement in the z-direction.

476 Fig. 5. Propagation of the elastic waves in the 2D axle section and their interference with the flaw.

477 Fig. 6. Displacement waves with crack and without crack at the position of detection

478 Fig. 7. Test item (a) and defect positions (b).

479 Fig. 8. Scheme of the laser-ultrasonic scanning system.

480 Fig. 9. The laser-ultrasonic experimental set-up.

481 Fig. 10. The laser-ultrasonic scanning system.

482 Fig. 11. The laser ultrasonic experimental set-up for the sensitivity analysis to sound-probe distance

483 (a) and probe angular position (b).

484 Fig. 12. Ultrasonic signal RMS variation with respect to source-probe distance (a, probe angular

485 position 6 deg) and probe angular position (b, source-probe distance 32 mm).

486 Fig. 13. Ultrasonic time history at the minimum (32 mm, dashed line) and the maximum (247 mm,

487 solid line) source-probe distance.

488 Fig. 14. Time histories (a) and (b), experimental set-up scheme (c) and B-scan (d) – D1.

489 Fig. 15. B-scan close-up around the Rayleigh wave time of arrival – Defect D1.

490 Fig. 16. Experimental set-up scheme (a), (c), (e) and B-scan (b) (d), (f) for defects D2, D3, D4

491 respectively.

Fig. 1. Schematic view
[Click here to download high resolution image](#)

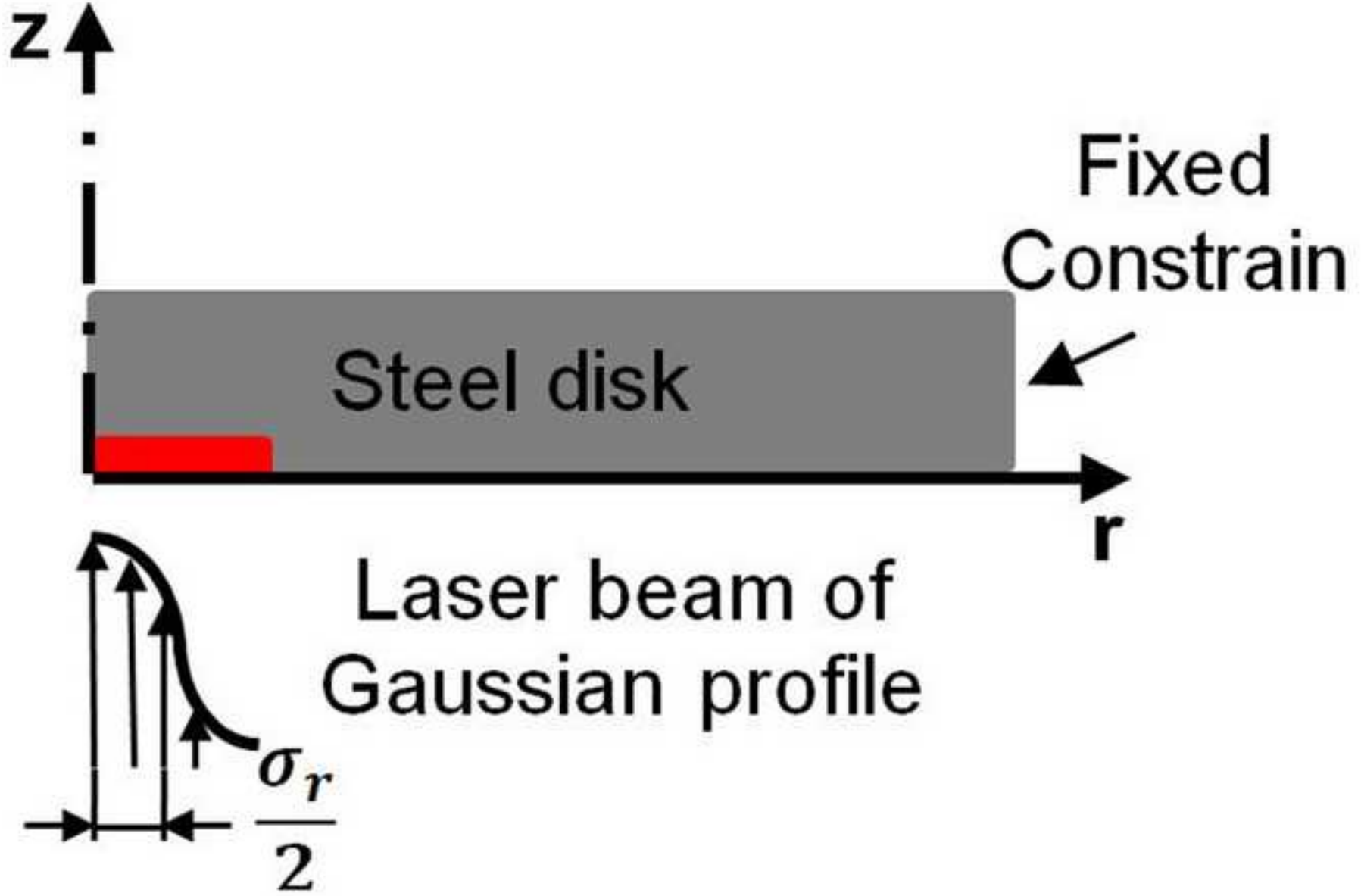


Fig. 2. 3D visualization of the propagation of the elastic waves
[Click here to download high resolution image](#)

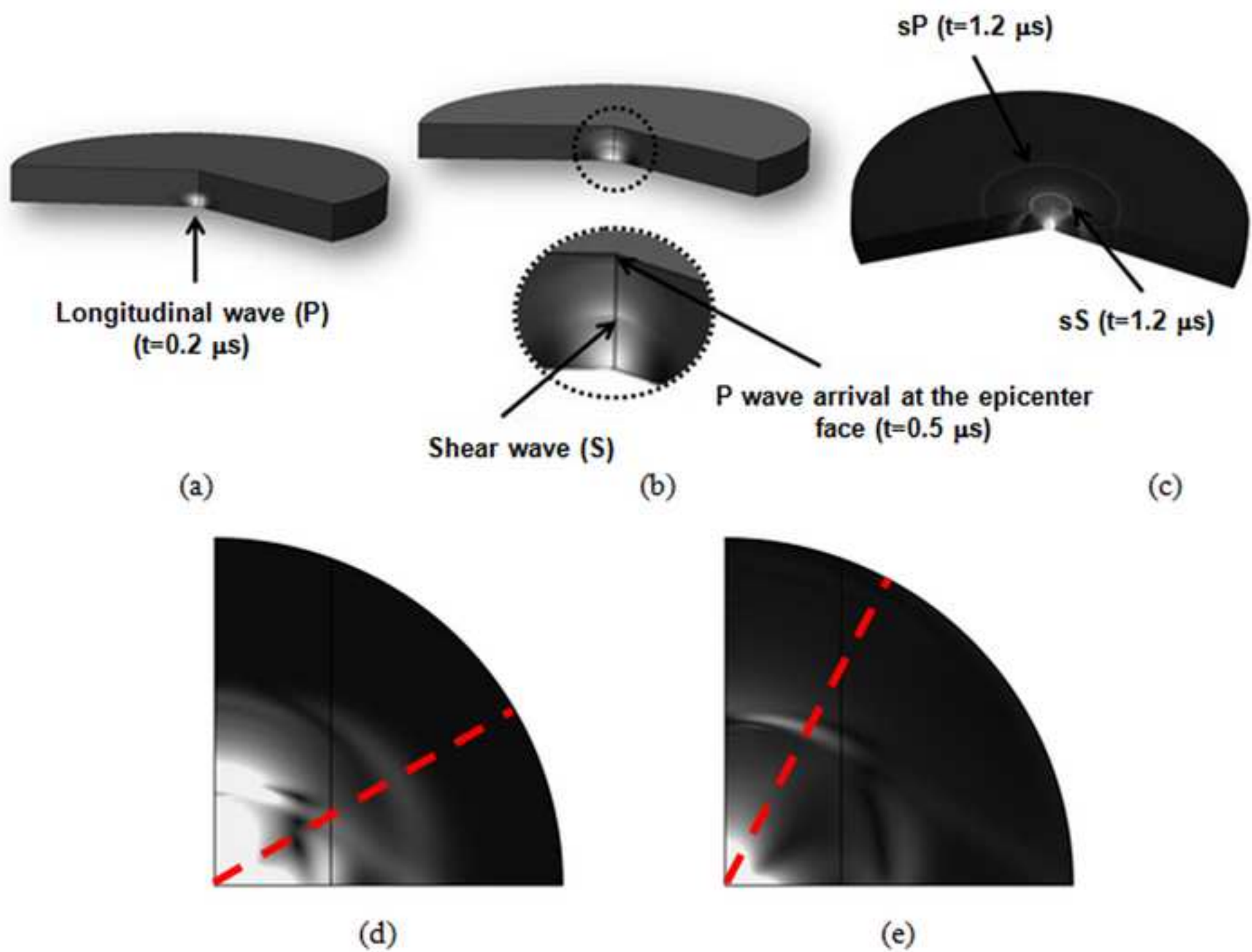


Fig. 3. Experimental set-up
[Click here to download high resolution image](#)

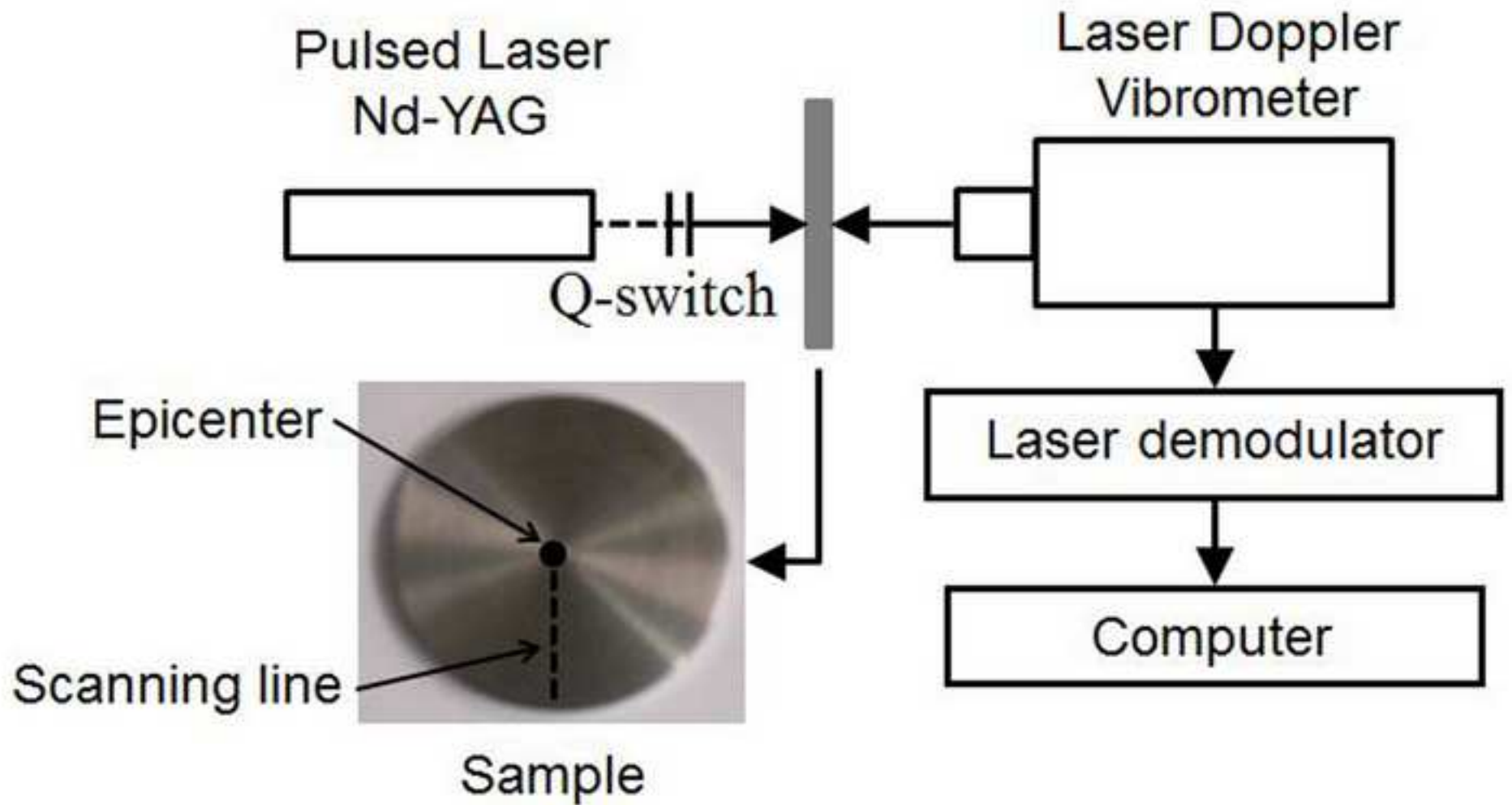


Fig. 4. Waterfall of the numerical (a)
[Click here to download high resolution image](#)

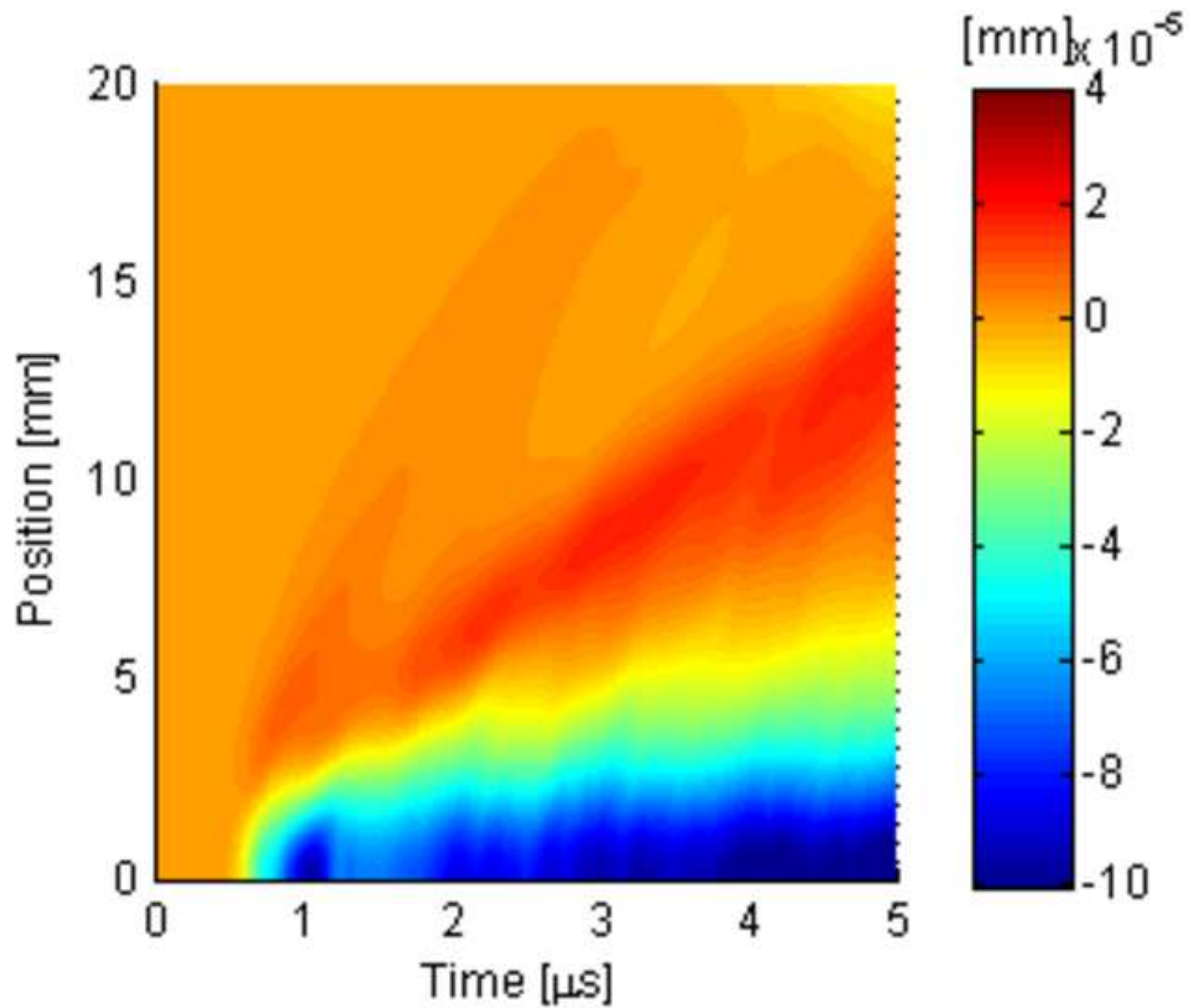


Fig. 4. Waterfall of the numerical (b)
[Click here to download high resolution image](#)

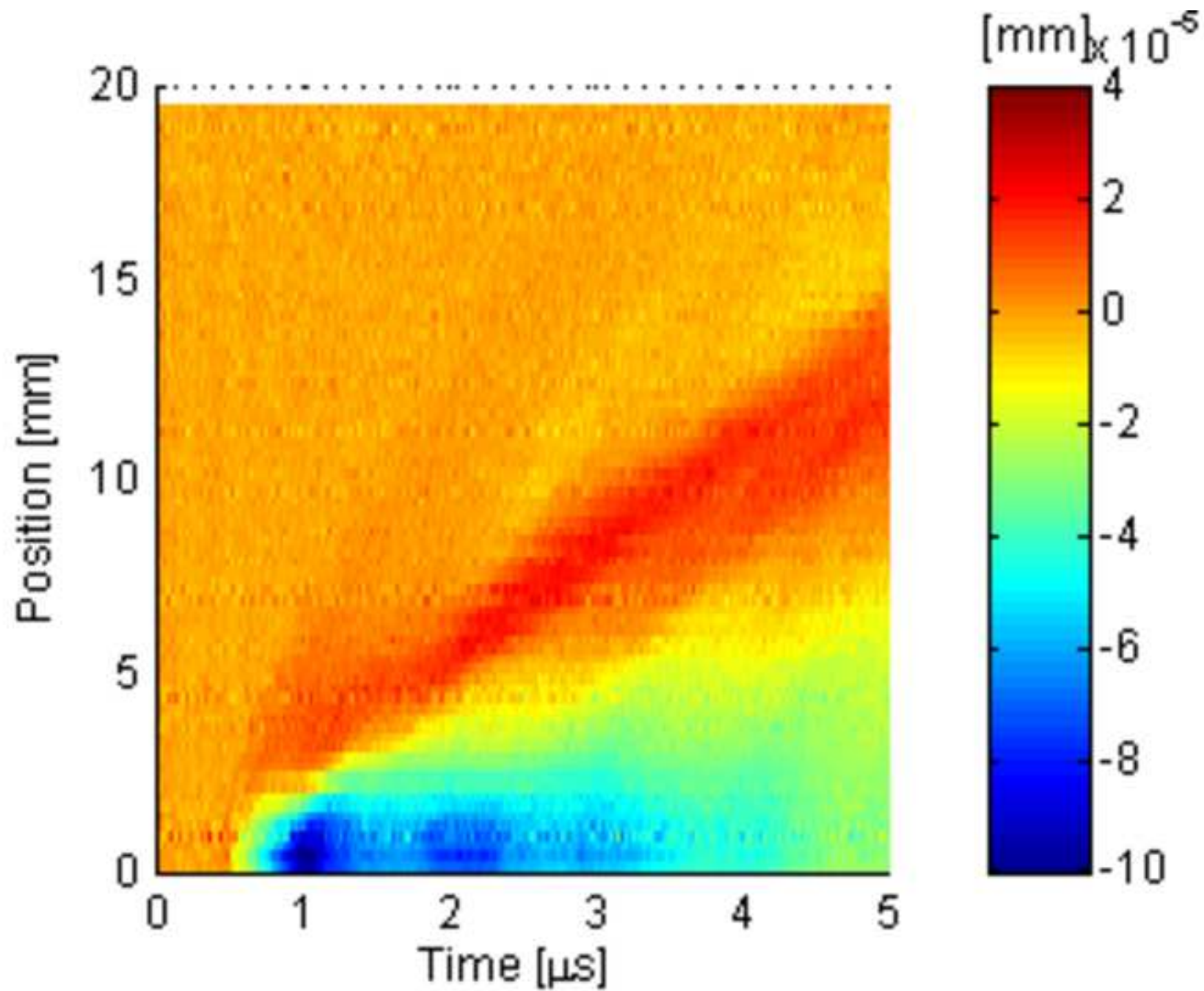


Fig. 5. Propagation of the elastic waves
[Click here to download high resolution image](#)

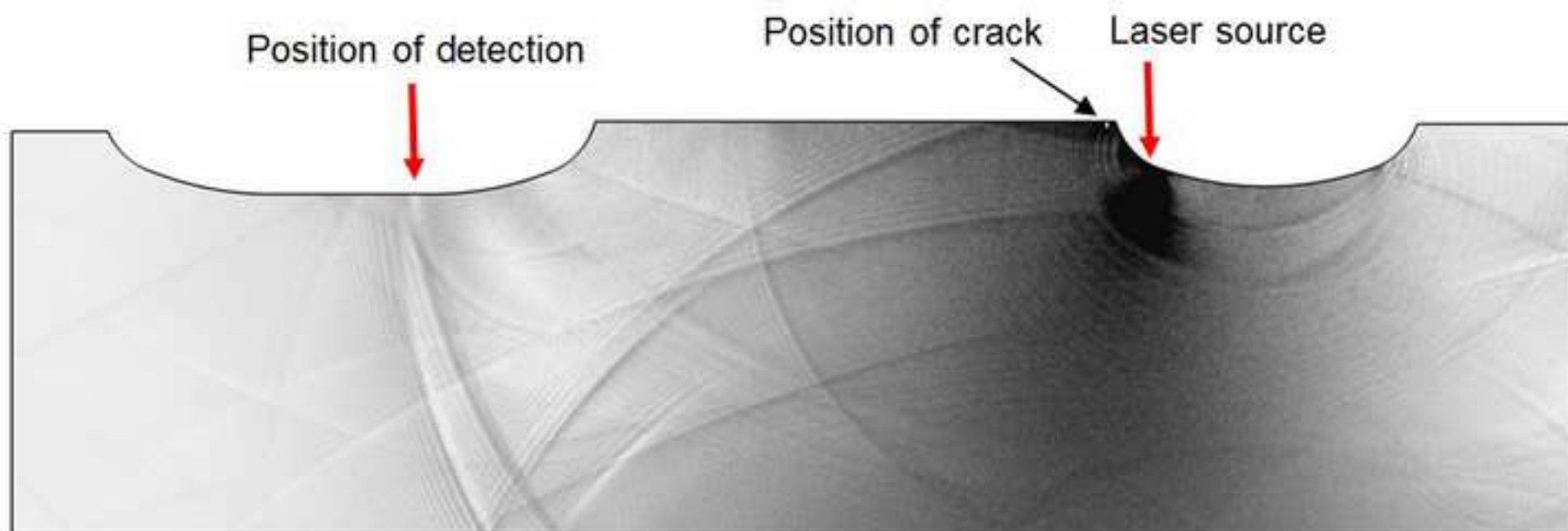


Fig. 6. Displacement waves
[Click here to download high resolution image](#)

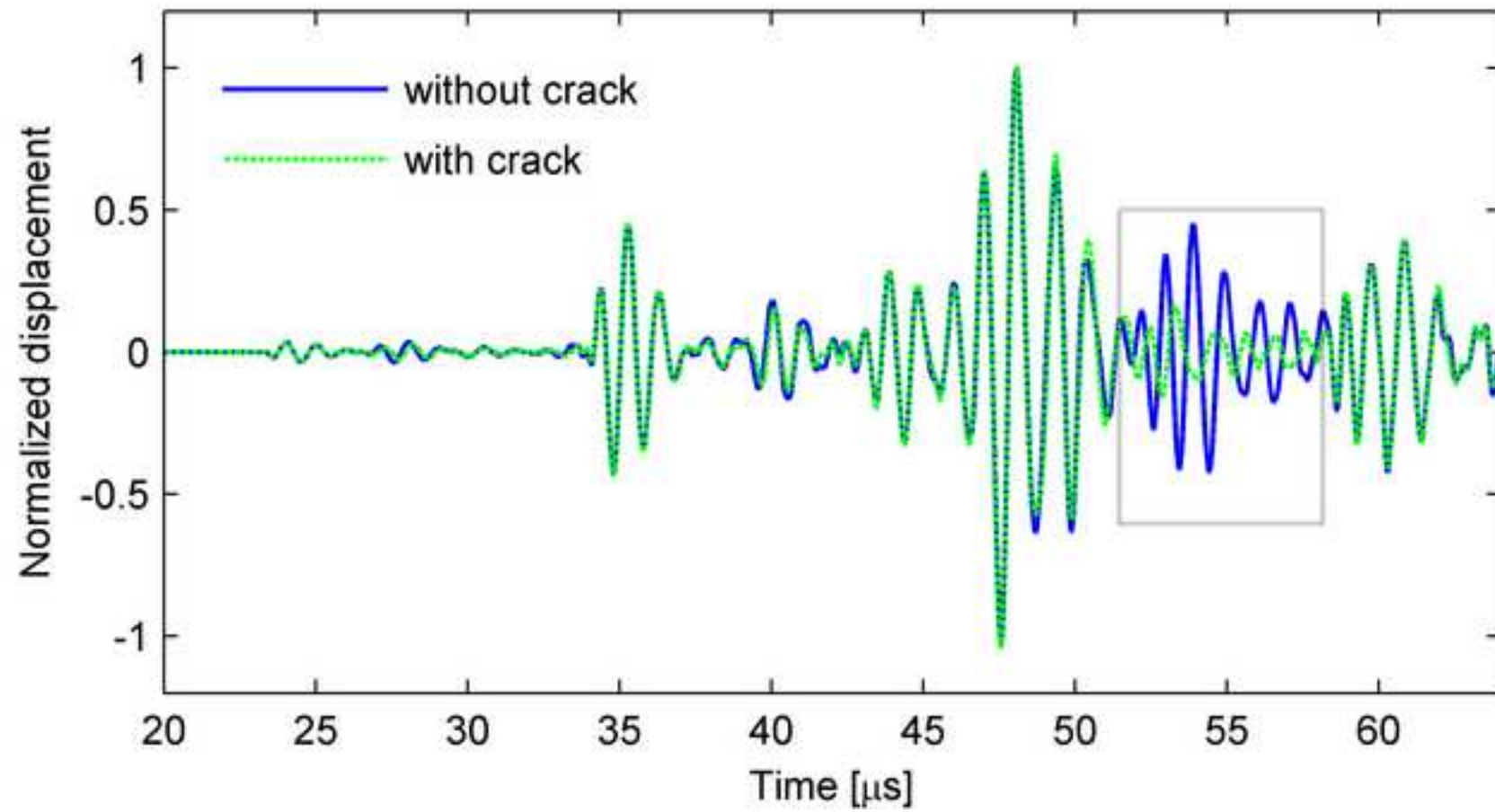


Fig. 7. Test item

[Click here to download high resolution image](#)

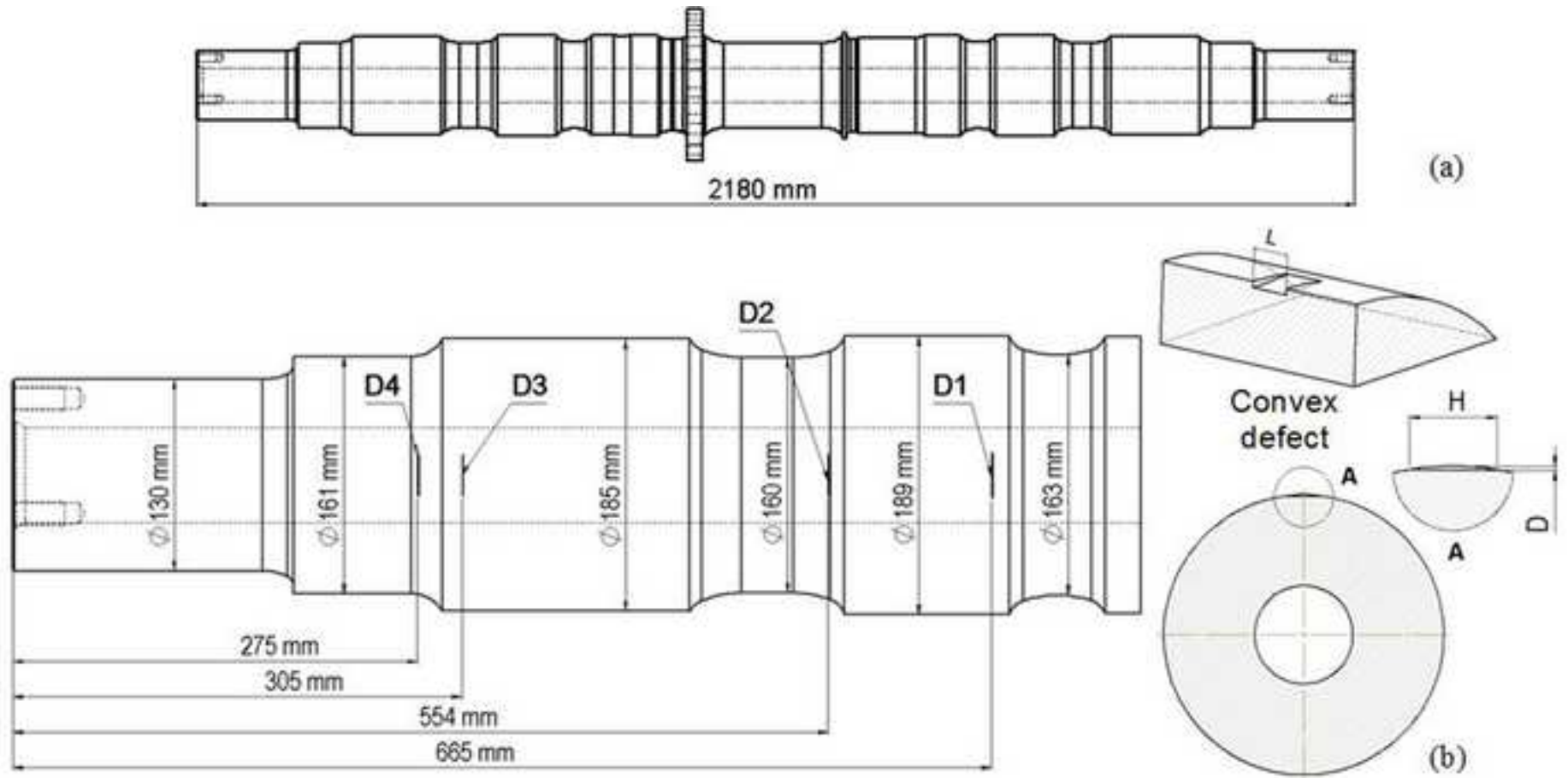


Fig. 8. Scheme of laser-ultrasonics scanning system.
[Click here to download high resolution image](#)

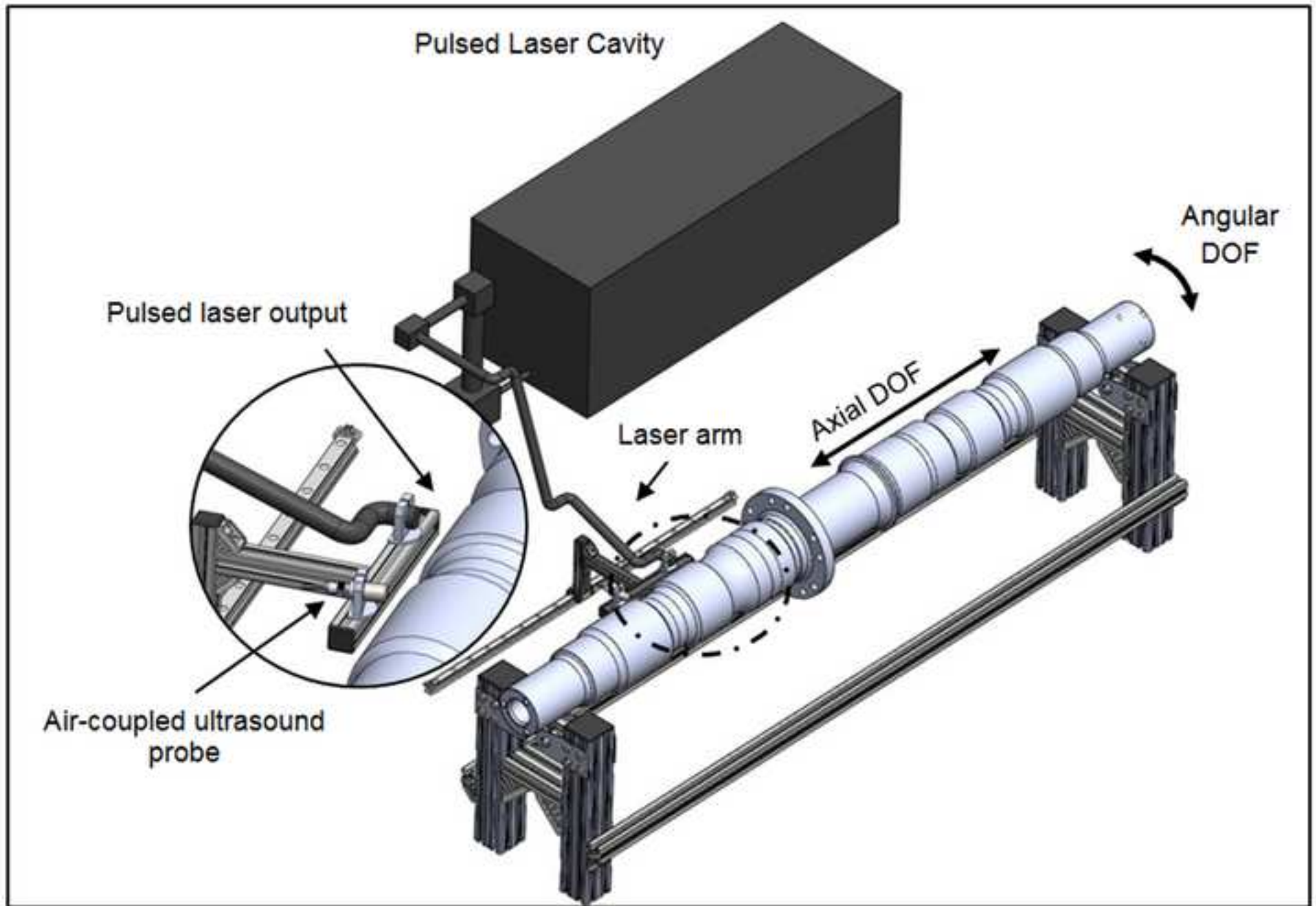


Fig. 9. The laser-ultrasonics experimental set-up.
[Click here to download high resolution image](#)

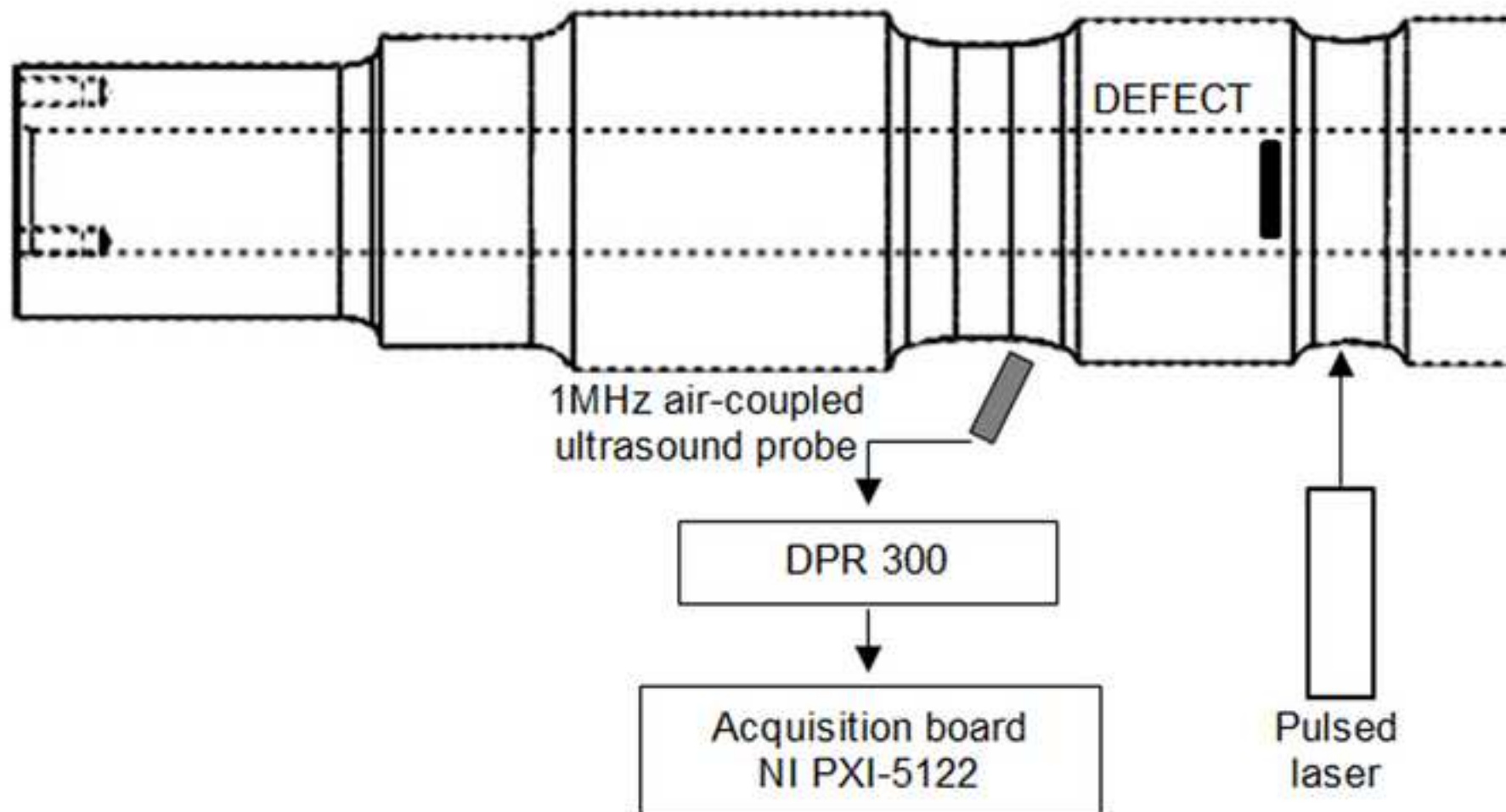


Fig. 10. The laser-ultrasonic
[Click here to download high resolution image](#)

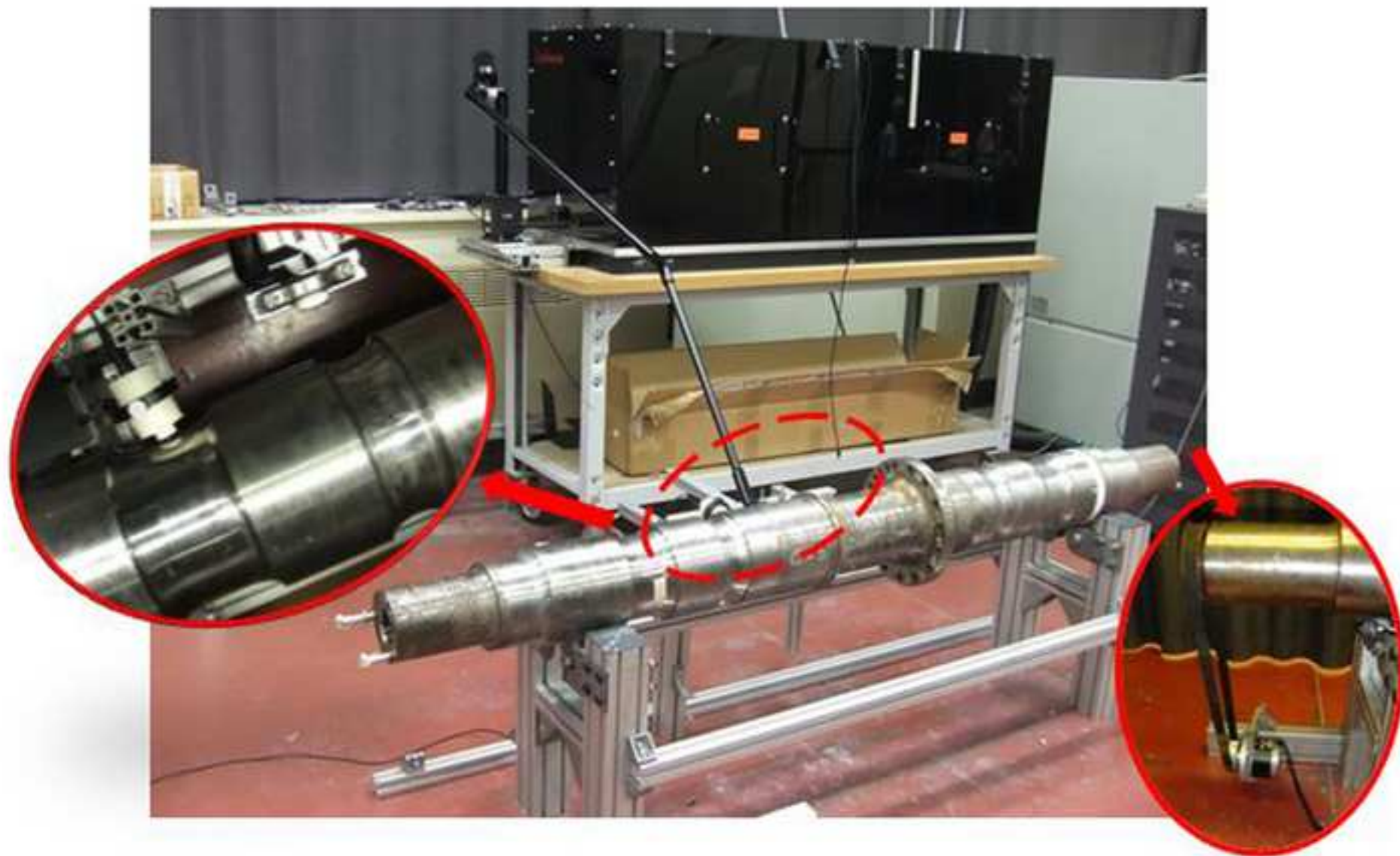


Fig. 11. The laser ultrasonics experimental set-up
[Click here to download high resolution image](#)

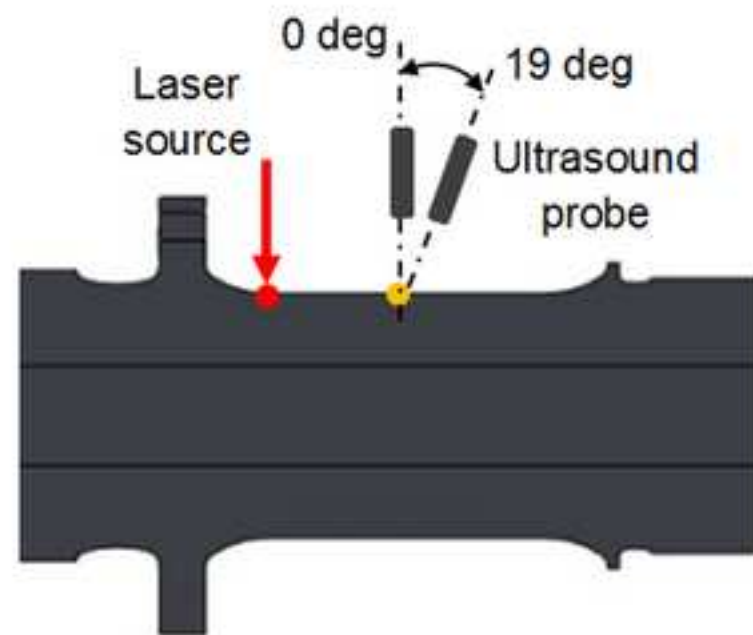
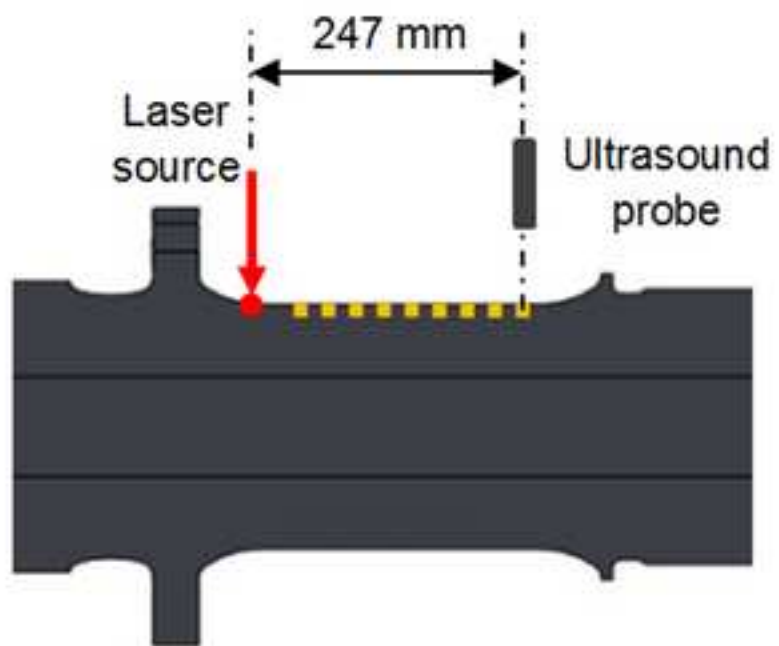


Fig. 12. Ultrasonic signal RMS variation
[Click here to download high resolution image](#)

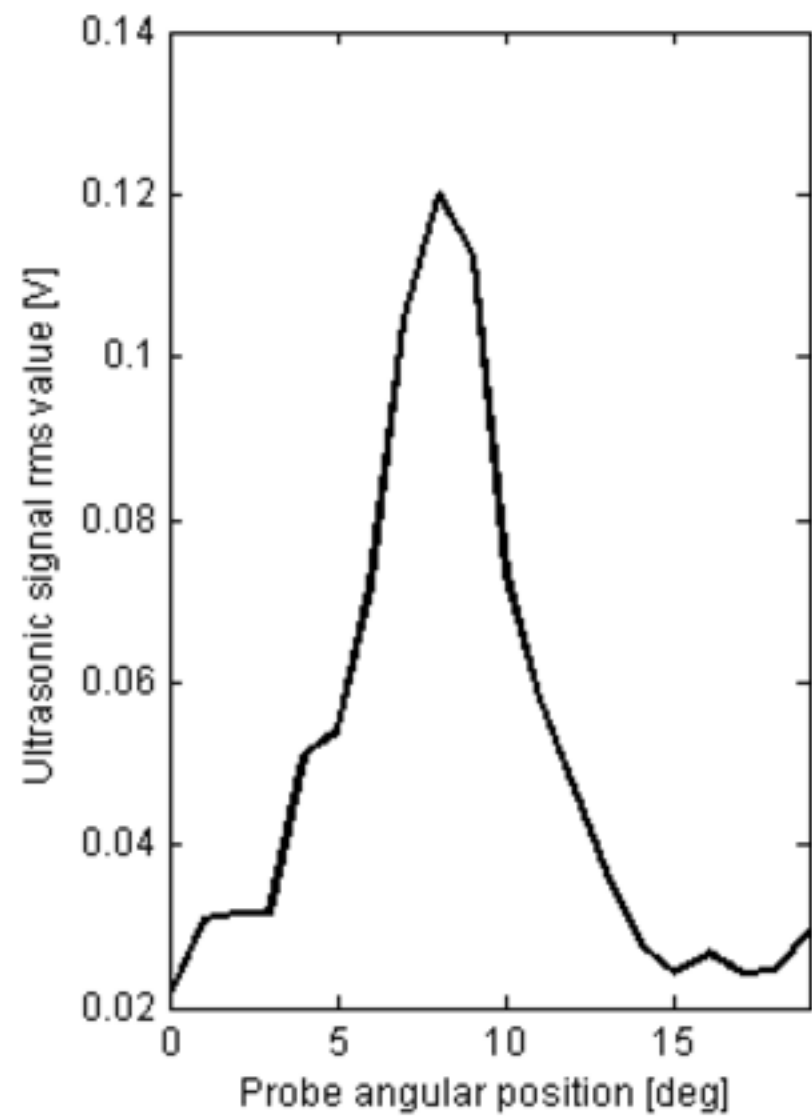
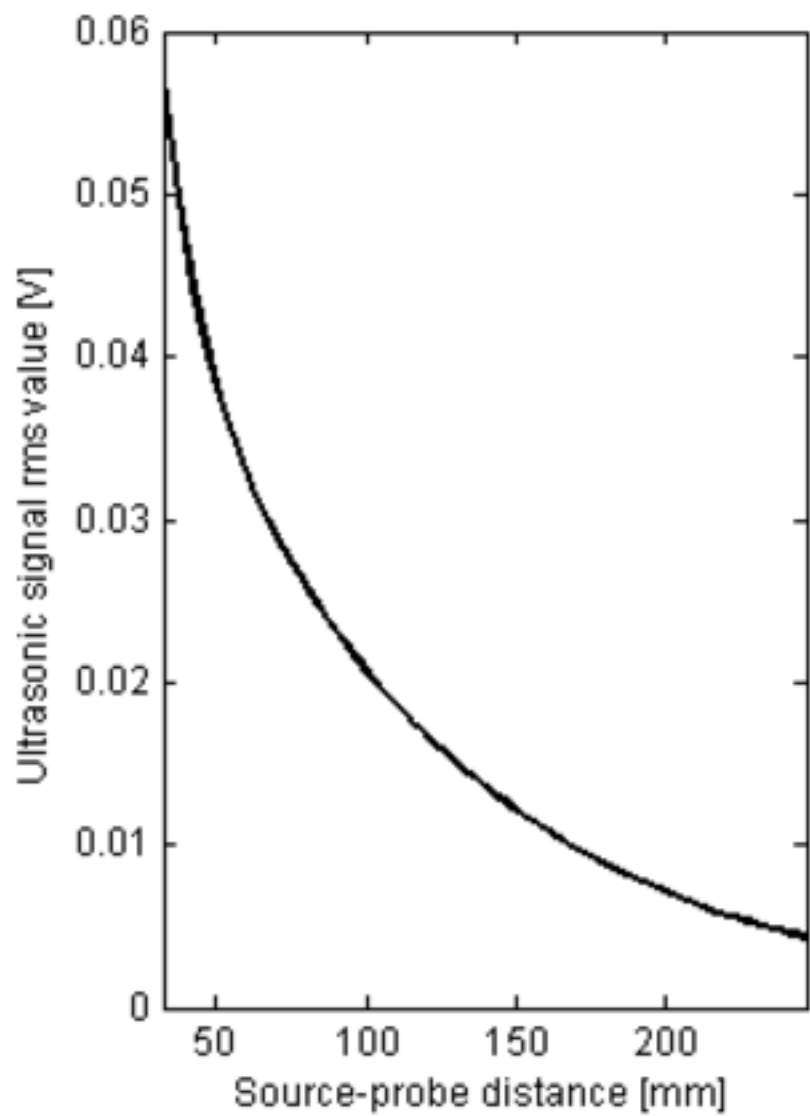


Fig. 13. Ultrasonic time history
[Click here to download high resolution image](#)

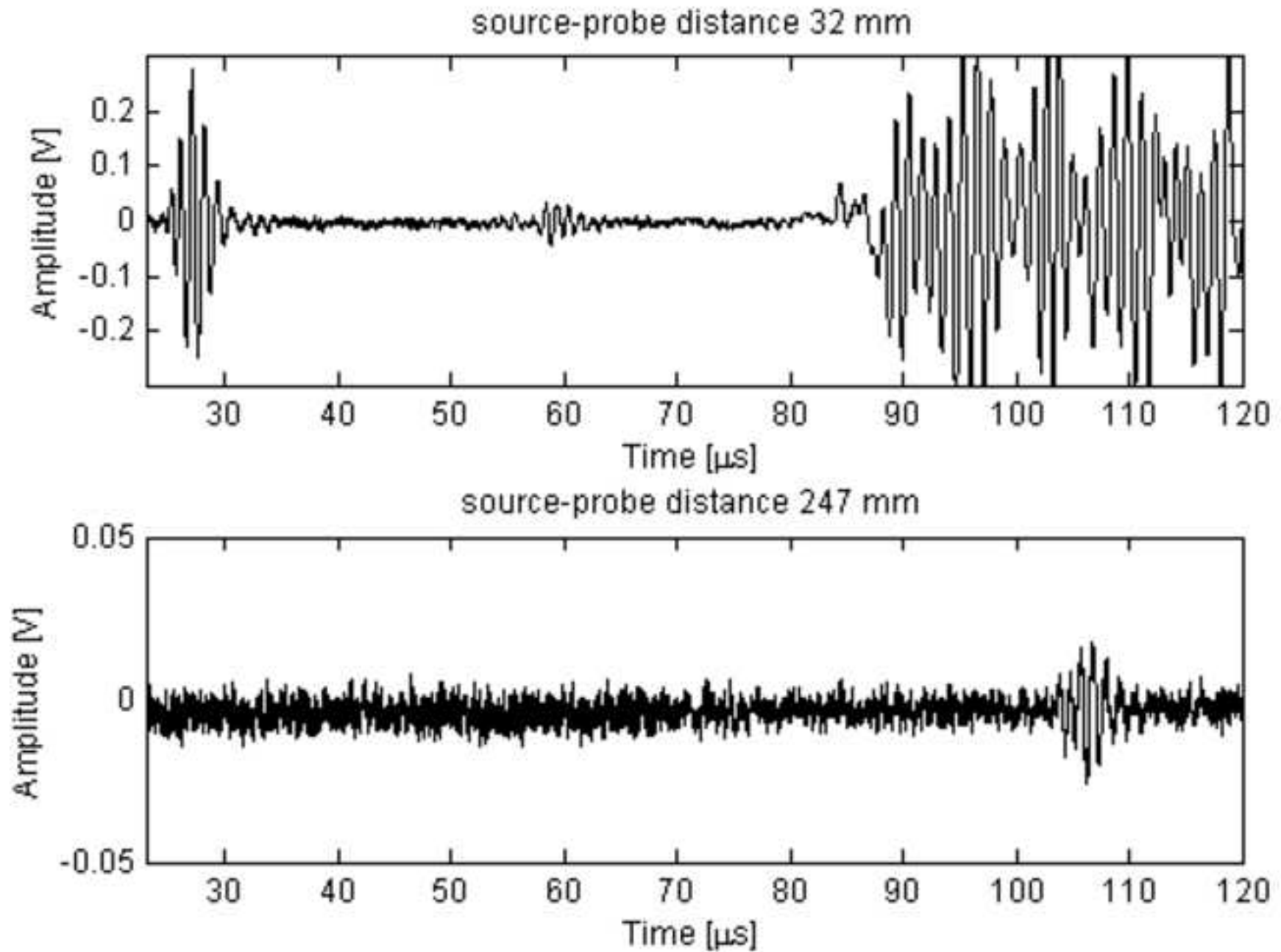
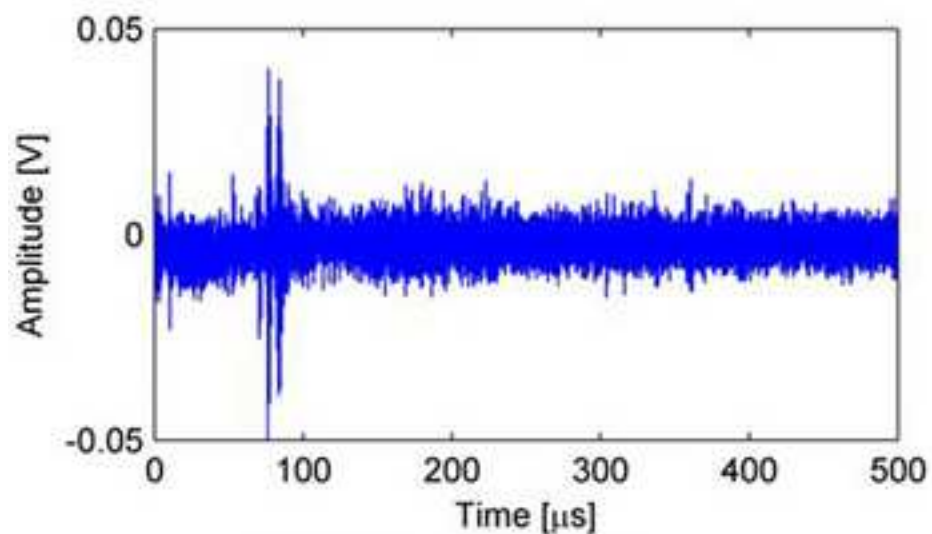
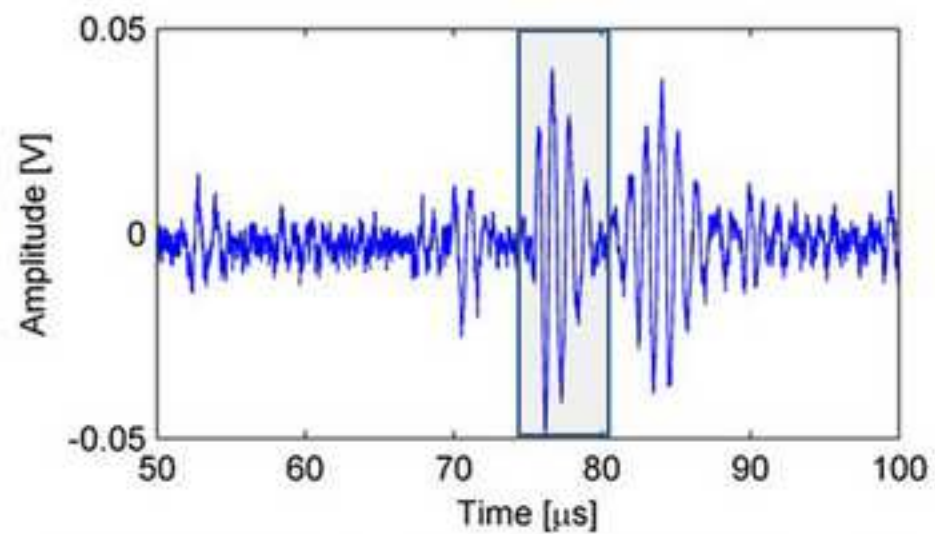


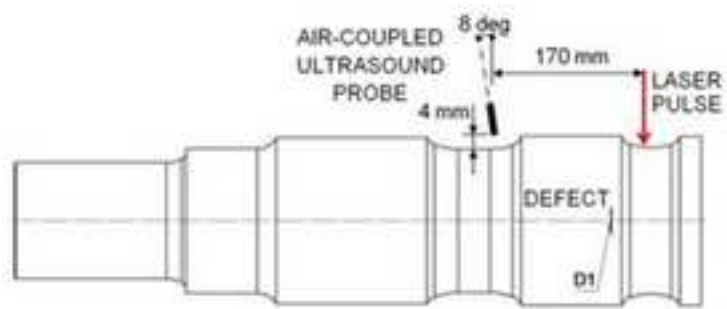
Fig. 14. Time histories
[Click here to download high resolution image](#)



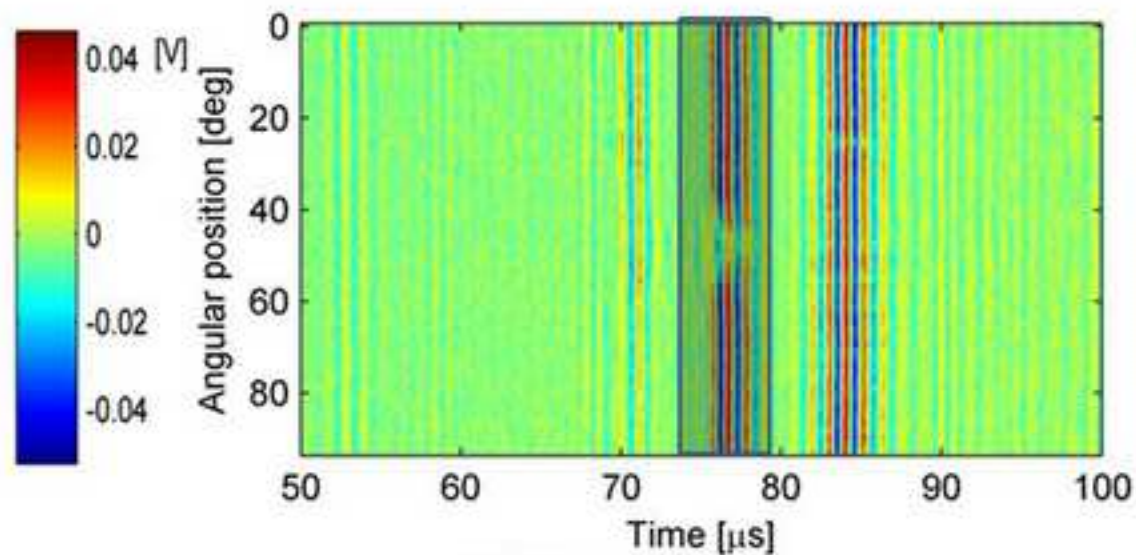
(a) Entire time history



(b) Time history close-up on the bulk waves



(c) Experimental set-up



(d) B-scan

Fig. 15. B-scan close-up around the Rayleigh wave.
[Click here to download high resolution image](#)

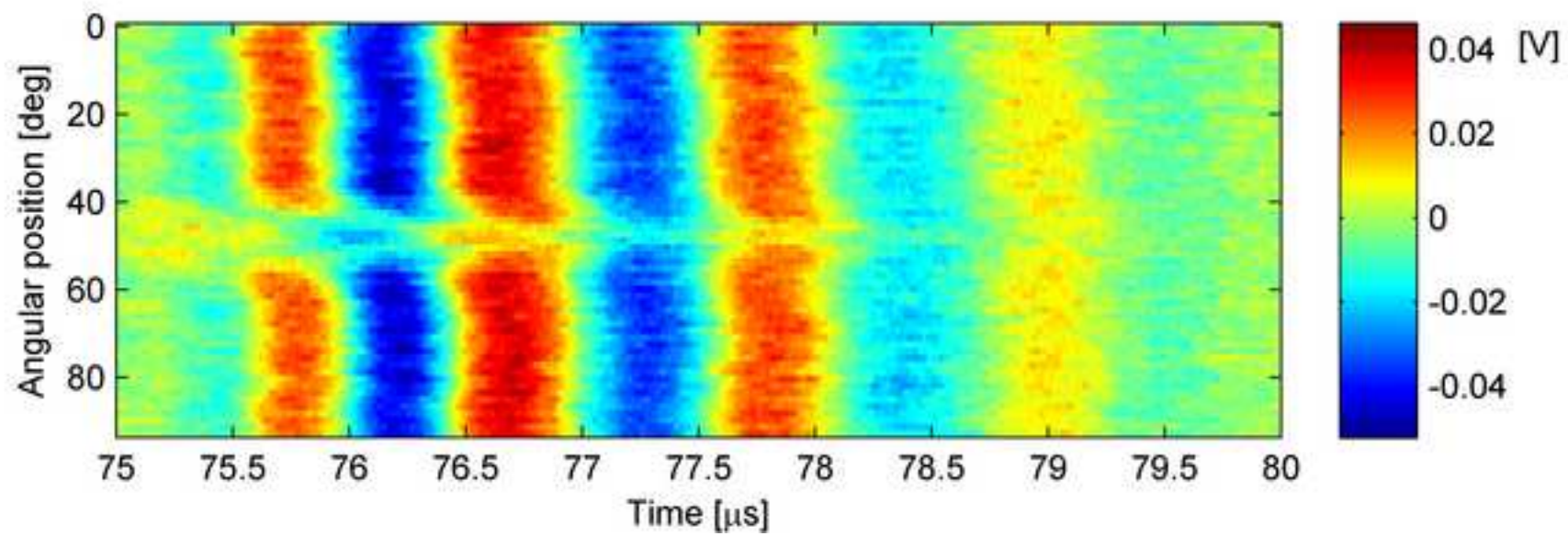
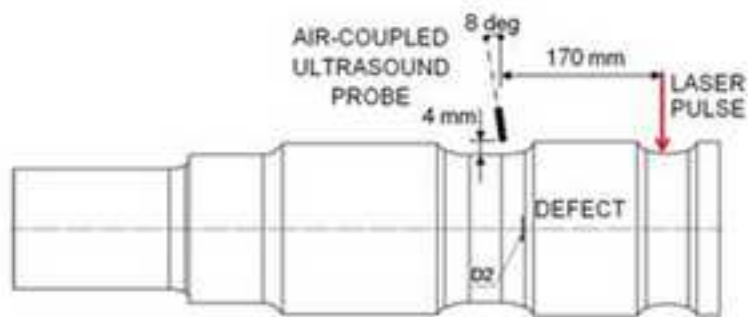
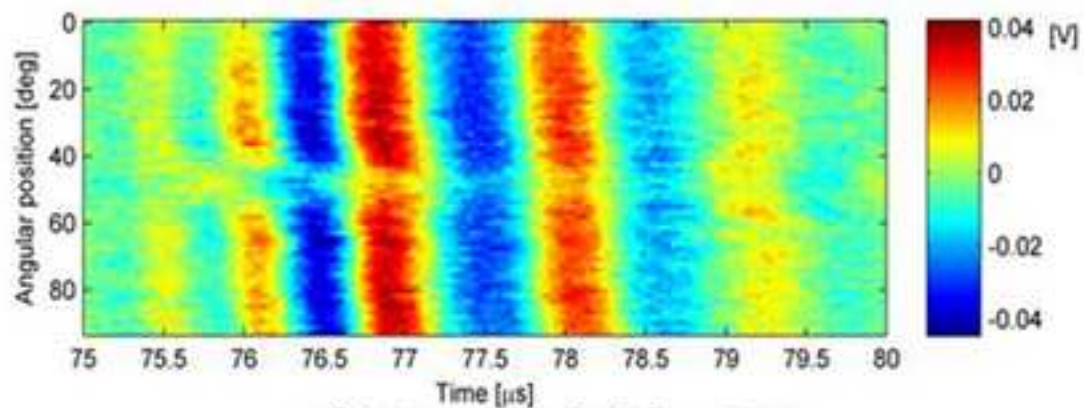


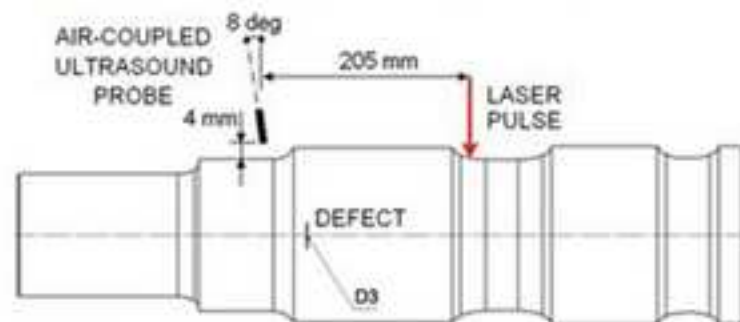
Fig. 16. Experimental set-up scheme
[Click here to download high resolution image](#)



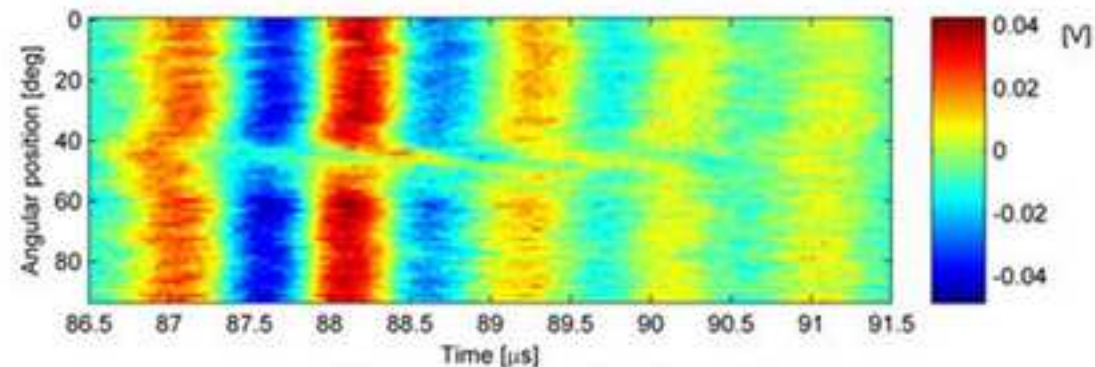
(a) Experimental set-up - defect D2



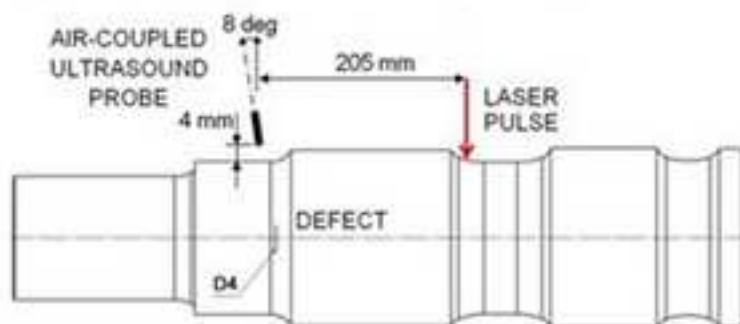
(b) B-scan of defect D2



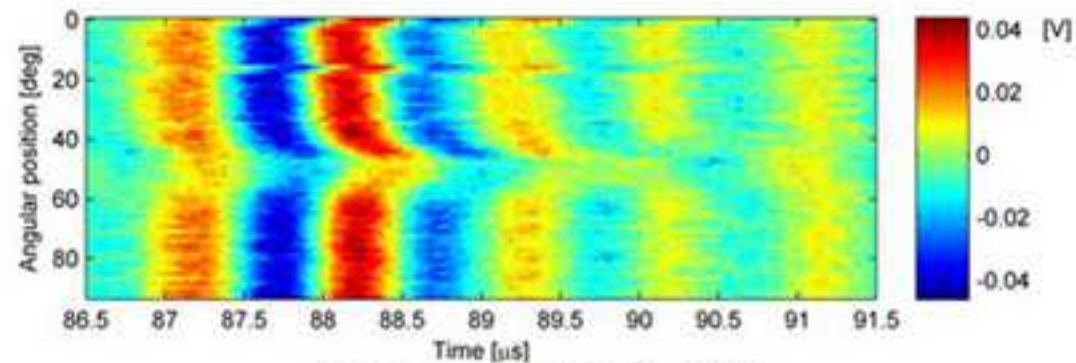
(c) Experimental set-up - defect D3



(d) B-scan of defect D3



(e) Experimental set-up - defect D4



(f) B-scan of defect D4

Table 1 Steel mechanical/thermal/optical properties.

ρ	Density	7900 kg/m ³
E	Young Modulus (@ 273.15 K)	200 GPa
C	Specific heat capacity	480 J/(kg K)
k	Thermal conductivity	50 W/(m K)
α	Coefficient of thermal expansion	10.7 e ⁻⁵ K ⁻¹
R	Reflection coefficient	0.3
A_c	Absorption coefficient	3.87 e ⁹ m ⁻¹

Table 1 Defect morphology.

Defects	Size of defect		
	H (mm)	L (mm)	D Max depth (mm)
D1	31	1.1	1
D2	28	1.1	1
D3	28	1.1	1
D4	28	1.1	1

Highlights

- A laser-ultrasonics procedure for train axles ultrasonic inspection is reported.
- A FE model for the design of experiments based on laser-ultrasonics is described.
- A sensitivity analysis to the angular position and distance was performed.
- The experimental tests was able to identify the presence of defects.